Review

Clay-Supported Metal Oxide Nanoparticles in Catalytic Advanced Oxidation Processes: A Review

Is Fatimah [1],*, **Ganjar Fadillah** [1], **Ika Yanti** [1] **and Ruey-an Doong** [2],*

[1] Department of Chemistry, Faculty of Mathematics and Natural Sciences, Universitas Islam Indonesia, Kampus Terpadu UII, Jl. Kaliurang Km 14, Yogyakarta 55112, Indonesia; ganjar.fadillah@uii.ac.id (G.F.); ika.yanti@uii.ac.id (I.Y.)

[2] Institute of Analytical and Environmental Sciences, National Tsing Hua University, Hsinchu 30013, Taiwan

* Correspondence: isfatimah@uii.ac.id (I.F.); radoong@mx.nthu.edu.tw (R.-a.D.)

Abstract: Advanced oxidation processes (AOPs) utilizing heterogeneous catalysts have attracted great attention in the last decade. The use of solid catalysts, including metal and metal oxide nanoparticle support materials, exhibited better performance compared with the use of homogeneous catalysts, which is mainly related to their stability in hostile environments and recyclability and reusability. Various solid supports have been reported to enhance the performance of metal and metal oxide catalysts for AOPs; undoubtedly, the utilization of clay as a support is the priority under consideration and has received intensive interest. This review provides up-to-date progress on the synthesis, features, and future perspectives of clay-supported metal and metal oxide for AOPs. The methods and characteristics of metal and metal oxide incorporated into the clay structure are strongly influenced by various factors in the synthesis, including the kind of clay mineral. In addition, the benefits of nanomaterials from a green chemistry perspective are key aspects for their further considerations in various applications. Special emphasis is given to the basic schemes for clay modifications and role of clay supports for the enhanced mechanism of AOPs. The scaling-up issue is suggested for being studied to further applications at industrial scale.

Keywords: advanced oxidation process; clay; metal nanoparticles; photocatalysis; nanoparticles

1. Introduction

Rapid developments in chemical industries enhance the quality of human life with the various products created for daily life, healthcare, building, electronics, etc. However, on the other hand, industrial activities lead to several problems related to industrial waste, including wastewater, which needs to be minimized and effectively handled without being discharged into the environment. Water scarcity problems, however, are being faced in India, China, and Thailand, as well as other countries. For example, the accessibility of safe drinking water in Indonesia is just 87.75%, and the rate can be as low as 66% in some African countries. It was reported that around 52% of rivers are heavily polluted, and India has 4% of global freshwater resources for drinking and food consumption; in addition, it was reported that about 70% of drinking water sources in China are polluted [1,2]. Moreover, water scarcity and crises are predicted to reach critical conditions as a global issue in 2025. Some studies have highlighted that trends in water scarcity are enforced by some factors, such as climate change, industrialization, food systems, country-level socio-economic systems, livelihoods and wellbeing, conflict and security, economies, and ecosystem interests [1]. Therefore, multidisciplinary approaches are required to minimize and overcome the issue. Water crises that are correlated with water contamination by hazardous substances from industrial activity need serious attention [3]. The effects of industrial waste and wastewater are mainly related to the chemicals' components having negative effects, due to carcinogenic, infectious, and toxic properties. Chemical-containing

wastewater is the main problem to be resolved for the sustainability of industries. Organic-containing wastewater from some industrial sectors represented a key interest for water quality management considerations. The potential persistence, toxicity, carcinogenic, and detrimental impacts of organic compounds utilized in many strategic sectors are the main reasons. For example, from industrial textile activities, over 20% of the dye consumed during production is released as a major component in wastewater [4]. In other sectors, pharmaceutical industries have an E-factor between 50 and 100 kg/kg of desired product correlated with many steps within the process, which are mainly organic and volatile organic compounds. The persistent character of compounds from industrial wastewater has necessitated the development of and exploration for effective and efficient treatment methods over recent decades.

Some conventional methods, such as chemical precipitation, coagulation, flocculation, adsorption, and membrane filtration, are well-known technologies which have applied for many years; however, the effectiveness is still low in terms of perspectives and challenges for sustainable technology and future perspectives [5,6]. As an illustration, coagulation and flocculation require high volumes of consumable chemicals as coagulants and flocculants which are not reusable. This contributes to the high cost of using industrial products, not only for the amounts consumed in production, but also for handling by-products and end-products [7]. Another example is adsorption mechanisms; although the adsorbents are advantageous because of their reusability, adsorbents have limited effectiveness against low concentrations of pollutants, and the recycling is dependent on adsorbent lifetimes; an adsorption capacity is also required [8]. Advanced oxidation processes (AOPs), including chemical oxidation and photocatalytic oxidation, as well as their intensified mechanisms, such as ozone-induced oxidation, ultrasound-induced oxidation, and microwave-induced oxidation, have attracted attention as powerful methods for treating organic-compound-containing wastewater [9,10]. The potential complete oxidation of organic compound pollutants in water is an improvement to reduce the chemical consumption, regeneration, and cost of the treatment. The capability of catalysts to accelerate oxidation reactions plays a key role in the effectiveness of dyes and the removal of organic compounds [11,12].

From the perspective of green chemistry and the considerable efforts for improving the catalytic process, the use of metal and metal oxide nanoparticles for advanced oxidation processes was developed. Nano-sized metal and metal oxides lead to enhanced and more efficient catalytic interactions compared with their bulk forms, and their unique characteristics make them the most versatile class of materials with properties covering all aspects of their applications [13,14]. Within this scheme, some metal oxide semiconductors were reported to have excellent catalytic activity for such oxidation process. However, some problems encountered by the use of nanoparticle forms include: (i) stability in hostile environments, especially in real and complex systems; (ii) toxicity caused by potential bioaccumulation; and (iii) regeneration and reuse technical procedures [15,16]. In vitro and in vivo studies indicate that reactive oxygen species (ROS) are produced by the exposure of nanoparticles, which is a predominant mechanism leading to toxicity. Immobilization and metal oxide nanoparticle catalyst supports are approaches for suppressing these drawbacks [17,18]. Solid supports play important roles in supporting metal oxide nanoparticles, by positioning themselves as ligands and protectors for reactive and uncontrolled conditions; these can contribute to providing an active surface site which contribute directly to the reactivity.

Silica-alumina-based materials, as well as porous materials, have been reported to be good solid supports for many metal oxide catalysts and photocatalysts [17,19]. The capability of these materials for adsorbing target compounds is a distinct advantage for efficient mechanisms which are usually studied by such kinetics and mechanism models. Undoubtedly, using clay as a natural material has always been worthy of consideration and received intensive interests. This is also specifically due to the chemical structure of clay, which can be arranged in different schemes with other materials that have fixed porous structures, such as activated carbon or zeolite. The layered structure of the clay enables the

dispersion technique and mechanism to be adjusted according to the characteristics of the nanoparticles [20,21].

The use of clay minerals in catalysis itself has been recorded in oil industries since 1903. Clay structures provide surface acidity and porosity for surface mechanisms in catalytic cracking. Furthermore, many studies have recommended clay minerals as the ultimate choice for a catalyst support, due to their low cost, high mechanical and chemical stability, and environmentally friendly characteristics, including the metal and metal oxide nanoparticle catalysts [22–25].

This review is focused on clay-mineral-supported metal and metal oxide, according to the role of clay in various advanced oxidation-mechanism-based catalysis and photocatalysis processes. The study highlights the greenness of the processes, and is a fair comparison between the use of pure metal or metal nanoparticles with a clay-supported form, as well as the comparison with respect to other solid supports. Finally, the future perspectives and potential developments are presented.

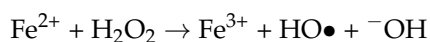## 2. Catalytic Advanced Oxidation Process for Water Treatment

Advanced oxidation processes (AOPs) are techniques based on the role of highly reactive species for oxidizing and degrading organic matter. The oxidation reactions are encompassed by the generation of highly reactive oxygen species (ROS), such as hydroxyl radicals (HO$^\bullet$), superoxide radicals (O$_2$$^{\bullet-}$), and singlet oxygen (^{1}O$_2$). In most cases, AOPs involve the generation of reactive species other than those which have been mentioned, including ozonide anions (O$_3$$^{\bullet-}$), hydroperoxyl (HO$_2$$^\bullet$), chlorine (Cl$^\bullet$), and sulphate (SO$_4$$^{\bullet-}$), and their radicals [26,27]. Furthermore, the mechanisms for producing those highly active ROS can be classified as chemical, electrochemical, photochemical, and sonochemical processes, as described in Figure 1.
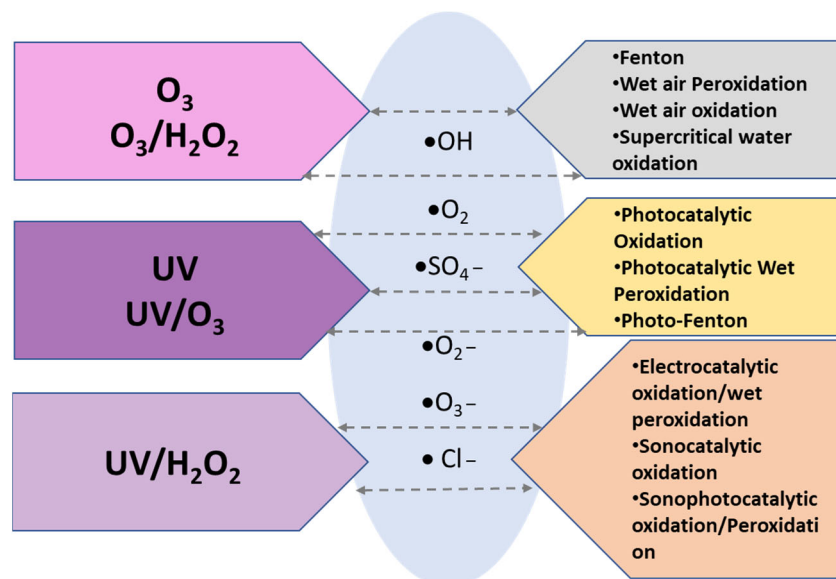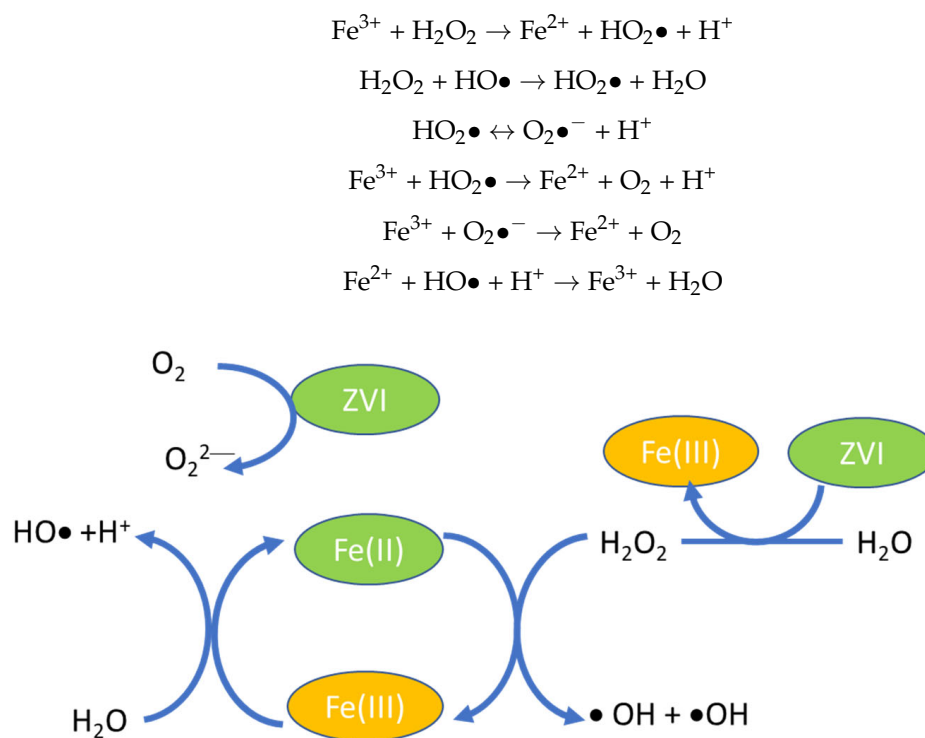

Figure 1. Various AOP methods.

Firstly, AOPs are known from the Fenton reaction, in which OH$\bullet$ and O$_2$$\bullet$$^-$ play roles in catalysis through the presence of homogeneous Fe^{2+} in the solution. In this classic mechanism, a mixture of Fe(II) and hydrogen peroxide generates OH$\bullet$, which leads to the production of HOO$\bullet$ and O$_2$$\bullet$$^-$, which is known as catalytic wet peroxidation (CWP). This mechanism can be applied for wet air and supercritical systems.

Figure 2 presents the scheme diagram of the reduction–oxidation steps:

$$Fe^{2+} + H_2O_2 \rightarrow Fe^{3+} + HO\bullet + {}^-OH$$

$$Fe^{3+} + H_2O_2 \rightarrow Fe^{2+} + HO_2\bullet + H^+$$

$$H_2O_2 + HO\bullet \rightarrow HO_2\bullet + H_2O$$

$$HO_2\bullet \leftrightarrow O_2\bullet^- + H^+$$

$$Fe^{3+} + HO_2\bullet \rightarrow Fe^{2+} + O_2 + H^+$$

$$Fe^{3+} + O_2\bullet^- \rightarrow Fe^{2+} + O_2$$

$$Fe^{2+} + HO\bullet + H^+ \rightarrow Fe^{3+} + H_2O$$

Figure 2. Diagram of the reduction–oxidation by Fe^{2+}/Fe^{3+}.

For most cases of organic-polluted wastewater, advanced sulfate-radical-based oxidation processes (SR-AOPs) have received increasing attention due to their advantages, such a longer lifetime compared with hydroxyl radicals (HO•). Sulfate radicals ($SO_4\bullet^-$) have a notably high reduction potential (2.5–3.1 V vs. NHE) and are stable at a wide range of pH values [28]. The mechanism involves peroxydisulfate (PDS, $S_2O_8^{2-}$) and peroxymonosulfate anions (PMS, HSO_5^-) as the radical precursors for producing sulfate radicals through the presence of UV, heat, metal ions, ozone, alkaline solution, metal ions, and metal oxide semiconductors. Various transition metal ions, such as Fe(II), Fe(III), Co(II), Ru(III), Mn(II), Ni(I), Ag(I), and V(III), have been reported as effective PDS/PMS initiators, or as catalysts for catalytic oxidation [29,30]. It was noted that Co(II), Ag(I), and Ru(III) are the most effective catalysts for PDS activation; however, their high prices make them not applicable in practical water treatments. In terms of the economic considerations, Fe(II) and Fe(III) are the most commonly selected catalysts [31].

With the rapid advancements in catalytic techniques, there has been considerable focus on the use of various metal oxides as oxidant catalysts instead of Fe(II) and Fe(III) ions for all ROS generation mechanisms [24]. Such problems faced by the use of iron catalysts are related to corrosive properties in excessive oxygen, especially for the harsh conditions involved in wet air and supercritical processes. High pressure and temperature can easily induce corrosion problems which lead to a shorter catalyst reactor life [32,33]. On the other hand, precipitation potentially occurs, along with reduced catalyst activity. Due to severe drawbacks of the use of iron ions in homogeneous catalysis, including the lack of recoverability of the catalyst used, the replacement of homogeneous catalysts with heterogeneous forms is a growing concern. To date, the most widely applied AOPs include heterogeneous Fenton reactions, photo-Fenton reactions, catalytic wet peroxide oxidation, heterogeneous photocatalytic oxidation, catalytic ozonation, and electrochemical oxidation. Numerous other successful materials have demonstrated oxidative activity, including MnO_2, Fe_2O_3, Fe_3O_4, TiO_2, MnO_2, NiO, ZnO, and SnO_2 [5,34,35].

Figure 3 presents the popularity of metal oxides in AOPs observed based on publications during 2019–2020.
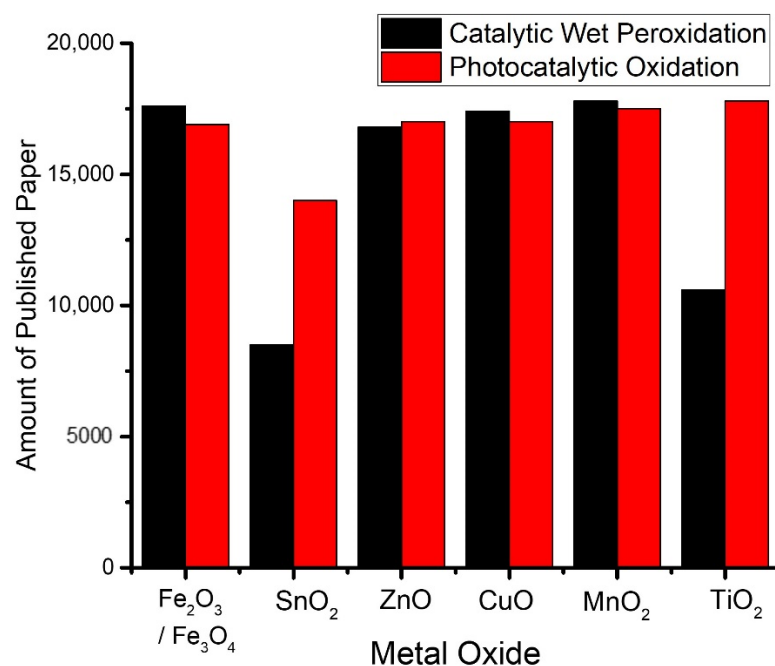
Figure 3. The popularity of metal oxides in AOPs observed based on publications during 2019–2020.

Manganese oxide in various phases was highlighted to be a potential catalyst with a similar activity to iron-based catalysts. The possible structures of manganese oxide are α-Mn$_2$O, α-MnOOH, β-MnOOH, γ-MnOOH, and Mn$_3$O$_4$, which influence the activity for ROS production, including PDS/PMS activation [36,37]. A notably high activity of α-MnO$_2$ was recorded as the complete oxidation of phenol was attained in short-term catalytic oxidation. The enhanced reactivity of α-Mn$_2$O$_3$ is related to its high specific surface area and higher amounts of low-coordinated surface oxygen sites, which are capable of facilitating the activation of oxygen and improving the surface redox properties. For photocatalysis schemes, TiO$_2$ is the most popular material [38,39].

3. Metal and Metal Oxide Nanoparticles in AOPs

Nanomaterials and nanoparticles are at the forefront of material research and have wide applications, due to distinct properties such as better optical, magnetic, catalytic, and electronic characteristics than those of bulk or individual atoms. Metal nanoparticles exhibit larger surface-to-volume ratios as compared with their bulk equivalents, which makes them more efficient and attractive in these applications.

Further developments were addressed to the enhanced catalytic and photocatalytic activity of those metal oxides in nanoparticle forms, including the use of some metal nanoparticles such as Ni NPs, Fe NPs, Au NPs, and their metal oxide phases [40–45]. Size effects are of great interest in many studies and conclusively indicate that the shape and size of nanoparticles are responsible for the increasing activity of reactions involving oxidation capabilities. Studies on oxidation by iron oxide nanoparticles in comparison with bulk iron oxide have revealed that different mechanisms occur on the surface. Oxidation by bulk iron oxide begins with the formation of FeO along with reduced concentrations of metallic irons; furthermore, the surface will be converted to Fe$_2$O$_3$ and Fe$_3$O$_4$ which remain as the dominant species [46]. The oxidation over iron oxide nanoparticles is noticeably different, in that the initial stage of oxidation will produce FeO on the surface which will further be oxidized almost completely to Fe$_2$O$_3$. These different compositions of oxides on the surface determine the more responsive surface of the nanoparticles [47]. The popularity of metal oxide nanoparticles exhibits the same trend as that presented in Figure 3, which shows that TiO$_2$ NPs are the most attractive in AOPs. The applicability of TiO$_2$ NPs for the photocatalytic oxidation of a wide range of organic and inorganic contaminants in water has been well-recognized. Some benefits of the use of TiO$_2$ NPs are related to their band

gap energy, non-toxicity, and stability. In addition to TiO$_2$ NPs, many studies have also highlighted the activity of other metal oxides such as ZnO NPs, MnO$_2$ NPs, and ZrO$_2$ NPs for AOPs. Some representative metal oxide nanoparticles for AOPs are detailed in Table 1.

Table 1. Metal oxide nanoparticles for AOP applications.

Metal/Metal Oxide	Precursor and Synthesis Method	Remark	Reference
Mn$_3$O$_4$	Precursor of MnCl$_2$, by the precipitation method	Particle sizes of Mn$_3$O$_4$ nanoparticles are 20–35 nm, Mn$_3$O$_4$ NPs show high activity for the 99.9% degradation of methylene blue by photooxidation	[48]
ZnO	Zinc acetate precipitation method	ZnO NPs show a removal efficiency of reactive blue of 85.4%	[49]
γ-Fe$_2$O$_3$	Synthesized using FeSO$_4$·7H$_2$O by the precipitation method	γ-Fe$_2$O$_3$ NP sizes of 40–50 nm with a phenol degradation activity of 94.5% within 420 min at 80 °C. The NPs shows reusability until the fifth cycle	[50]
α-Fe$_2$O$_3$	α-Fe$_2$O$_3$ NPs were in nanocubic form, prepared using a metal-ion-mediated hydrothermal route.	α-Fe$_2$O$_3$ NPs showed photocatalytic activity in rhodamine B degradation	[51]
CuO	CuO NPs were prepared by reflux and precipitation methods, followed by calcination at different temperatures of 350–550 °C. Particle's sizes are in the range of 17–34 nm, depending on method and calcination temperature	The highest activity of CuO NPs was exhibited by the NPs prepared by the reflux method and calcined at 450 °C. The highest degradation efficiency toward phenol was 95%. Nanoparticles showed stability until the third cycle	[52]
SnO$_2$	SnO$_2$ in nanosphere form was synthesized through a solvothermal method by a SnCl$_2$ precursor	The highest degradation efficiency of rhodamine B was 99% during 90 min under UV light	[53]

Various methods for metal and metal oxide nanoparticles have been reported, highlighting the different forms, crystallinity, particle size, and electronic state of the nanostructures, which affects their catalytic/photocatalytic activity. Their nanostructures can be divided into zero-dimensional (0D), one-dimensional (1D), two-dimensional (2D), and three-dimensional (3D). Each of these nanostructures can be subdivided into quantum dot arrays, planar arrays, elongated arrays, and ordered structures, respectively.

As examples, Figure 4 shows the morphologies of zinc oxides with nanorod, nanoflower, and nanosphere morphologies [54–57].

The morphologies and particle sizes are generally governed by crystal growth kinetics and mechanisms which are directed by the synthesis method. There are various synthesis methods for metal or metal oxide nanoparticles, which are mostly dependent on the characteristics of metal or metal oxide precursor. Sol–gel, emulsion, and precipitation are synthesis mechanisms and are intensified by various techniques such as hydrothermal, solvothermal, and mechanochemical treatment. For example, in the synthesis of ZnO nanospheres, precipitation reactions can be achieved with zinc acetate and NaOH as precursors through the following reaction:

$$Zn(CH\,COO)_2 + NaOH \rightarrow Zn(OH)_2 + CH\,COONa$$

$$Zn(OH)_2 \rightarrow ZnO + H_2O$$
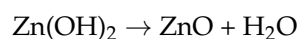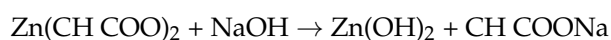
The nanospheres were obtained with different particle sizes through different techniques: hydrothermal and solvothermal [61]. For some metal oxide nanoparticles, the precursor determines the optimum synthesis method; for example, in the synthesis of TiO$_2$

using titanium alkoxide, the sol–gel mechanism is the better pathway because fast gelation of the precursor can affect the aggregation and prevent the formation of nanoparticles. Other characteristics, such as corrosivity, as well as oxidizable and degradable properties of the precursor, need to be concerned.
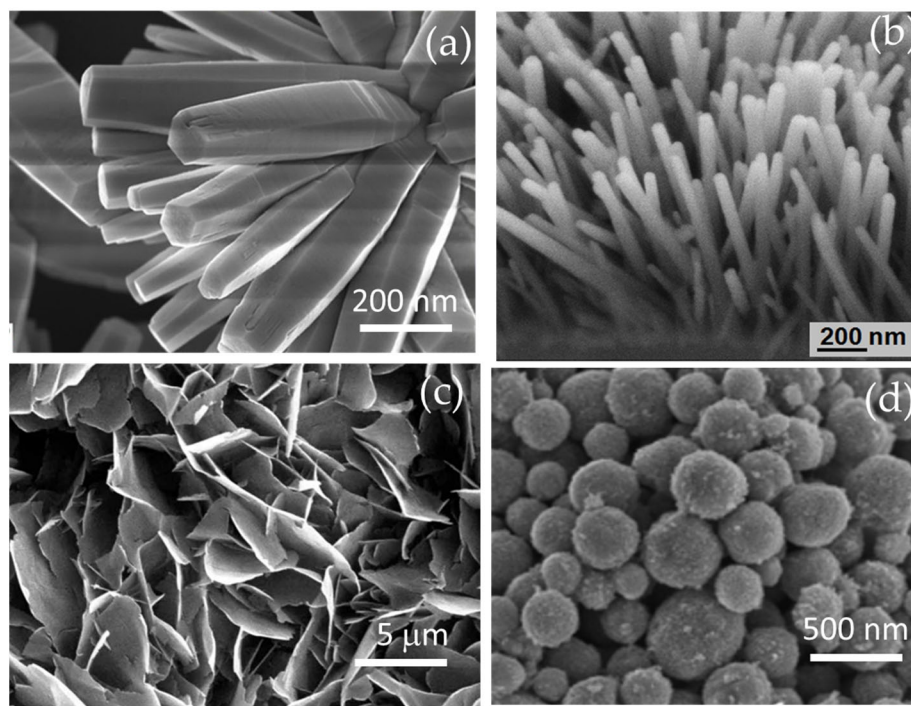
Figure 4. ZnO (**a**) nanoflowers, (**b**) nanorods, (**c**) nanoflakes, and (**d**) nanospheres. Reproduced from ref. [54,58–60] with permission from the publishers (Springer Nature, 2015; PLOS ONE, 2020; Science Publication, 2009; IOP Publishing, 2020).

Further considerations are growing concerning potential environmental impacts associated with the potential toxicity towards ecosystem damage and human health. The much higher reactivity of nanoparticles compared with bulk forms. which is influenced by the particle size that facilitates their transport through cell membranes, is a characteristic which needs risk assessment. [62,63]. Nanoparticle immobilization into stable and supportive solids is one of the strategies for preventing their release into the environment; moreover, metal and metal oxide incorporation with inorganic solids to form nanocomposites can enhance the reusability and recyclability of the catalyst without losing activity. Some research has evaluated the increased catalytic efficiency related to the cost-effectiveness and catalyst capabilities. For example, the dispersion of Pt nanoparticles into mesoporous Co_3O_4 was reported to increase the catalytic oxidative degradation efficiency toward methylene blue (MB) dye, with almost 100% removal after 60 min of treatment [64,65]. Similar results were recorded from supported ZnO nanoparticles using zeolite [66,67], supported iron nanoparticles using zeolite [68,69], and supported Au nanoparticles into TiO_2 and $BiVO_4$ [70,71]. Microporous and mesoporous solids were employed for supporting metal and metal oxide nanoparticles; some of them are noted to be low-cost supports such as zeolite, silica, graphene, carbon, C_3N_4, and clay minerals [72–76]. Especially for photocatalytic mechanisms, the enhanced activity and stability of metal or metal oxide nanoparticles can be attributed to the charge separation mechanisms provided by the solid support. Improvements in the sorption capacity are common benefits from the porous structure of the support. In addition, the capability of the surface to adopt the metal ions is notable. The presence of functional groups associated with hydroxyls bound on carbon material is an example which can be achieved by the utilization of biomass-based support [75]. In γ-Fe_2O_3/graphene oxide (GO), the enhanced photo-Fenton activity, as identified by the

accelerated Fenton-like mechanism, is caused by charge separation between g-Fe_2O_3 and GO [75].

Supports with a high specific surface area tend to support catalysis via an adsorption mechanism. Activated carbon is one of the verified supports for this model, because the supporting Au on activated carbon exhibits a higher turnover frequency (TOF) in catalytic phenol wet peroxidation and requires less H_2O_2 as an oxidant [77]. A similar role of the support was also demonstrated by clay in Fe/Cu/Zr-pillared clays for the catalytic wet peroxide oxidation (CWPO) of 4-nitrophenol (4-NP). The higher TOF was achieved with a smaller amount on the active catalytic site [78]. Interestingly, the synergic effect between active nanoparticles and the support leads to better reusability and recyclability [79–81].

4. Clay Structure and Utilization in Catalysis

Clays are silica alumina minerals with layered structures composed of aluminum silicates which are formed by tetrahedral and octahedral sheets, where the layers possess net negative charges and contain cations, such as Na^+, K^+, Ca^{2+}, etc., which occupy the interlamellar space. The amenability of clays for modification lies in the exchangeable properties of the cations; as such, they can easily be replaced by other cations or other molecules. The ion exchange mechanism and the layered structure govern the possible insertion of metal cations and molecules to be covalently anchored to layer atoms. The cation exchange capacity of clay is one of the factors affecting the modification mechanism, and is directly related to the clay structure, which depends on its chemical composition. In this regard, clay minerals are classified into different groups as follows: kaolinite, smectite, vermiculite, illite, and chlorite [82].

The smectite class of clay is the most popular for supporting metal and metal oxide catalysts, not only for advanced oxidation processes, but also for some catalyzed organic reactions. Smectite is composed of two layers of tetrahedral silica and one layer of octahedral alumina group, alternatively known as a 2:1 layer or T-O-T clay minerals, belonging to a group of hydroxyl alumino-silicates [83]. Smectites, which include montmorillonite, saponite beidellite, nantronite, and hectorite, are naturally formed from the weathering of soils or volcanic ash. The smectite group of clays is distinguished by differences in the chemical composition, with substitutions of Al^{3+} or Fe^{3+} for Si^{4+} in the tetrahedral cation sites and Fe^{2+}, Mg^{2+}, or Mn^{2+} for Al^{3+} in the octahedral cation sites [84].

Smectite structures increase swelling capabilities due to the high cation exchange capacity and ease to be hydrated. The thin layers and small particle sizes contribute to their high surface area; hence, they exhibit a high degree of absorbency of many materials, including organic compounds. Similarly, the structure is consistent for vermiculite, which is also 2:1 or T-O-T clay. Vermiculite differs from smectite due to its isomorphous substitution of higher-valence ions by lower-valence ions in the tetrahedral sheet (e.g., Al^{3+} for Si^{4+}) and in the octahedral sheet (e.g., Mg^{2+} or Fe^{2+} for Al^{3+}); thus, it has more negatively charged plate surfaces [85,86].

Different from smectite and vermiculite, kaolinite is a 1:1-type clay mineral which is composed of one layer of tetrahedral silica and one layer of an octahedral alumina group (T-O). Some minerals include kaolinite, nacrite, dickite, and halloysite, with a chemical formula of $Al_2O_3 \cdot 2SiO_2 \cdot 2H_2O$ (39% Al_2O_3, 46.5% SiO_2, and 14.0% H_2O) [87–89]. The structure possesses strong binding forces between the layers, causing less hydration or expansion resistance when wetted, a low specific surface area, and cation exchange capacity. Chlorite has a 2:1:1 structure with a sequence of T-O-T-O, and crystalline interlayer characteristics. Even though there is no possibility for intercalation, kaolinite and chlorite minerals have been reported to exert a capability to adsorb organic molecules and support metal and metal oxide nanoparticles.

Referring to the availability of pore structure, Brønsted and Lewis acid sites in clay structure, clays have been utilized in the beginning of petroleum refining and petrochemical industries. Kaolinite was the main clay mineral which was utilized in petroleum refining as active cracking catalyst [90]. Referring to the principle of heterogeneous catalysis, the

availability of porous structure in clay minerals can accelerate the reaction via surface mechanism. The cracking mechanism occurs and is controllable when the feed in gas phase is adsorbed on the catalyst surface, for furthermore breaking down into smaller molecules. The presence of Brønsted acid on the surface accelerates the cracking mechanism.

However, the lower stability of raw clay was found due to the loss of the surface area at high temperature-forced advanced modifications. Acid treatment and cation exchange processes were applied to clay in order to increase Brønsted or Lewis acidity, a procedure that was patented in 1949. In addition, for acid-catalyzed organic reaction, the selectivity to produce a certain product was the important feature to be concerned as well as total conversion of the reaction. The high specific surface area (SSA) and structure of clay minerals bring about the potencies to be modified and act as effective supports rather than its individual use. The benefit of previous reviews allows us to focus on material most relevant to modern, more relevant green/clean technologies. Metal modifications to clay structure, such as Pt-, Ni-, and Co- supported clay, were established as active catalysts in hydrocracking and hydroprocessing of fuel. Furthermore, clay modifications were performed in many schemes which were adapted to the reaction that will be catalyzed [91]. Functionalizations with basic modifier were attempted for base-catalyzed reactions, such as transesterification reaction, to produce biodiesel, for example, by supporting CaO and CaO/KF [92,93]. For other organic reactions with specificity and selectivity to produce a certain isomer, the inorganic complex immobilization was also reported, for example, Schiff base Pt(II)-complex intercalated montmorillonite. The catalyst showed 100% selectivity in producing 2,4-dinitrotoluene from the reduction of nitrobenzene [94]. The immobilization of metal complexes into clay structure, mainly the swelling clay, gave several advantageous related to the reusability, stereoselectivity, and minimizing radical mechanism that reduce applicability in producing selective product. Other examples for this are chiral bis(oxazaline)-copper (Box–Cu(II)) complexes supported on laponite clay for the addition of alkoxycarbonyl carbene-reaction [95], and ruthenium-complex intercalated saponite for citral conversion [96]. Until now, the study on clay functionalizations for organic reactions catalysis is still developing with various mechanisms with respect to the green chemistry principles consideration, including the metal and metal oxide nanoparticles modification which are reviewed in this paper.

5. Clay Modifications

There are some modification procedures to functionalize the clay surface. Below are some important schemes for this.

5.1. Impregnation

The dispersion of metal and metal oxide nanoparticles into non-swelling clays, such as kaolinite, halloysite, dickite, and nacrite, is usually conducted by the impregnation method, even though the procedure can also be conducted for swelling clay.

The impregnation mechanism depends on the metal precursor, and can be assisted by severe intensification procedures such as hydrothermal, microwave, and ultrasound irradiation. Various techniques, such as the sol–gel method, coprecipitation, wet impregnation, and their combinations, have been performed and chosen based on the technical characteristics of the metal precursor.

Sol–gel dispersion is usually performed because metal oxide formation can be achieved through polymerization in sol–gel systems. Pillarization by using organometal precursors, such as metal alkoxides (such as titanium isopropoxide, titanium isobutanate, and zirconium isopropoxide), and acetate salts, usually occur within this mechanism. Wet impregnation and coprecipitation are based on the homogeneously dispersed metal salt in the clay suspension, in which the coprecipitation conducted by the additive base environment forms the deposited metal hydroxide.

The dispersion of TiO_2 in kaolinite and hectorite using titanium isopropoxide can be conducted by a sol–gel mechanism due to Ti-O- bond formation via polymerization [88];

using different precursors, such as $TiOCl_2$ and $TiOSO_4$, the impregnation can be conducted by depositing titanium salt into clay suspension or through the coprecipitation method. Temperature, pH, and the precursor solvent are crucial factors in determining the particle size and distribution of the metal oxide in clay supports. Research on TiO_2/kaolinite using titanium isopropoxide demonstrated the role of the DMSO solvent in producing more space for the more homogeneous dispersion of TiO_2, which furthermore determines the hydrophobicity and reactivity of the nanocomposite [97]. The impregnation method including wet impregnation consists of mixing a precursor salt with a clay suspension in a solvent and tuning the optimum pH. As an example, the impregnation of TiO_2 into kaolinite utilizing $TiOSO_4$ was optimally conducted in an acidic mixture in order to maintain the ionic form of Ti^{4+} in the solution [98].

The coprecipitation method was reported in the synthesis of ZnO/montmorillonite. The combination of the sol–gel mechanism and wet impregnation method can also be conducted.

In a different scheme, the composite formation of MnO_2 nanosheets and MnO_2 nanowire with montmorillonite was achieved under hydrothermal conditions. For both inserted MnO_2 nanostructures, $KMnO_4$ solution was employed as a precursor and a hydrothermal procedure was conducted in a Teflon-lined stainless-steel autoclave. MnO_2 nanosheets were formed at 160 °C for 24 h over the mixture of the precursor solution and montmorillonite suspension. Meanwhile, for MnO_2 nanowire, a combination of $KMnO_4$ and $(NH_4)_2S_2O_8$ under hydrothermal treatment at 90 °C for 12 h was performed.

A decreased specific surface area was observed from both the nanostructure insertion to the montmorillonite structure, although a fast and efficient catalytic oxidation was reported. The catalytic activity is also subjected to the enhanced adsorption capacity caused by the surface oxide structure of the nanostructures [99]. The impregnation method does not guarantee a reduced specific surface area of the nanomaterial; however, in some cases, because the dispersed metal oxide is in the nanoparticle form, the increasing specific surface area related to the homogeneous surface dispersion results in more space formed on the surface. An increased specific surface area, about twice as large as that compared with the raw material, was recorded from the Fe_2O_3 nanoparticles deposited on kaolinite [100]. Figure 5 illustrates the possible formation of porous structure and new surfaces as adsorption sites by metal/metal oxide impregnation.
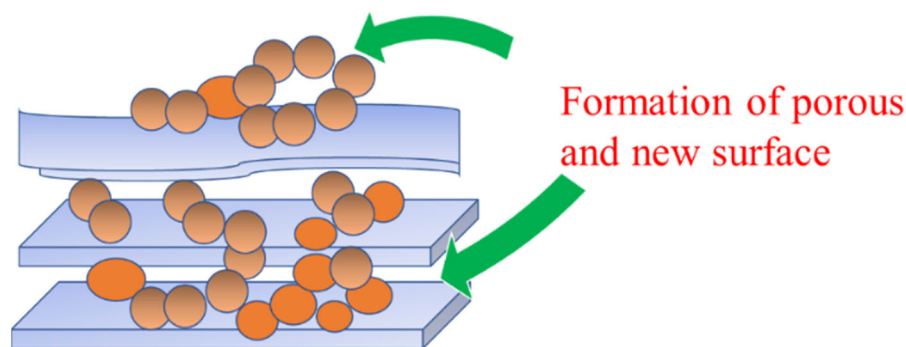

Figure 5. The possible formation of porous structures and new surfaces as adsorption sites by metal/metal oxide impregnation.

5.2. Pillarization

Pillarization is a popular mechanism of clay modification by metal oxide insertion to swelling clays such as smectite and vermiculite. The process consists of intercalation followed by a calcination procedure. Intercalation is an ion exchange process of native cations between the smectite layers with other cations having a higher reduction potential, or the polyoxocations [78,101]. The intercalation is intended to open up the interlayer region, creating a higher specific surface area or pore volume; furthermore, through the calcination process, dihydroxylation of the polyoxocations will produce a metal oxide as metal oxide pillars which is also homogeneously distributed metal oxide (Figure 6).

The stability of polyoxocations is the main factor for pillarization; therefore, the optimum conditions for some metal oxide pillaring precursors were studied. The polyoxocation of the Keggin ion Al_{13} is reported to be the best pillaring precursor for Al_2O_3, which can be prepared by the slow titration of Al salt with ^-OH at an Al:OH molar ratio of 1:1. With the same metal:OH molar ratio, the pillaring precursor for SnO_2 pillarization is synthesized by the mixing or slow titration of Sn salt with ^-OH with a final pH of 2, and Zr salt with ^-OH at a pH of 6–7.
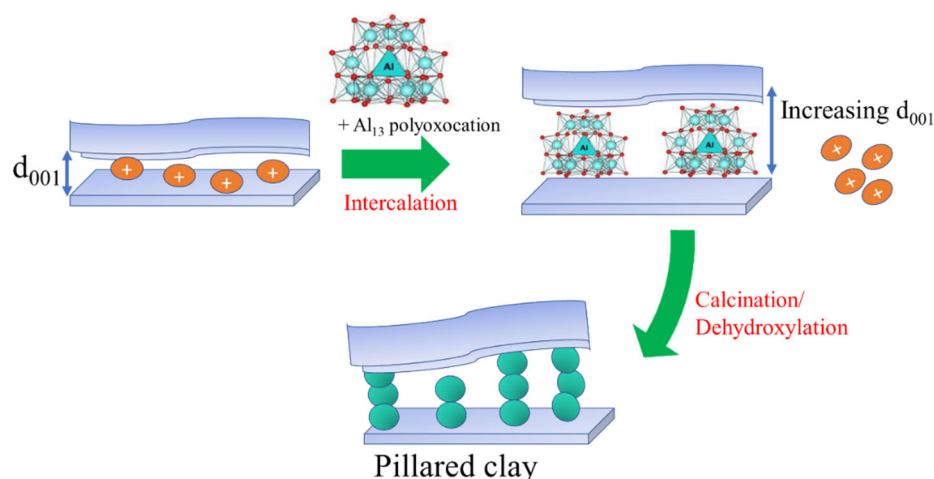
Figure 6. Schematic representation of clay pillarization.

The trimer $Sn_3(OH)_4{}^{2+}$ is the predominant species from the hydrolysis to construct stable SnO_2 in pillar formation [102]; meanwhile, the pillaring precursor for ZrO_2 is in the tetramer form $(Zr_4(OH)_{14}(H_2O)_{10})^+$ [103–105]. Different authors have demonstrated that the preparation of Fe-PILCs is affected by the OH:Fe molar ratio [105–109]. The polyoxocation of iron pillaring solution was obtained to have optimum polymerization at a pH of between 1 and 1.8; in addition, pH > 1.8 caused precipitation [110,111].

Pillaring species for titanium-pillared clay are still not exactly established. Some papers have conclusively suggested that in acidic environments, a polymeric $[(TiO)_8(OH)_{12}]^{4+}$ complex is the polyoxocation, and can be achieved with the utilization of $TiCl_4$. Another species is trimeric titanium hydroxide [85]. Various precursors and synthesis routes can be performed for the synthesis of titanium-pillared clay (Ti-PILC). $TiCl_4$, $TiCl_3$, $TiOCl_2$, titanium tetraisopropoxide, and tetrabutyl titanate have been reported as titania precursors [112,113]. The use of titanium tetraisopropoxide and tetrabutyl titanate was reported to be better in terms of specific surface area and clay structure compared with $TiCl_4$ and $TiOCl_2$. The milder condition achieved refers to the stability of $TiCl_4$ and $TiOCl_2$ at a very low pH, which potentially destroys the structure of clay minerals [85,114]. Conversely, the large Ti uptake in Ti-pillared clay was observed when using $TiCl_4$ as the intercalating agent; up to 55% as compared with the use of $Ti(EtO)_4$ and $Ti(isop)_4$ as precursors, which gave uptake values of TiO_2 of ~30%. As organo-titanium compounds, the interaction between precursors and native cations was not in ion exchange mode; thus, the release of exchangeable Ca^{2+} and Na^+ cations did not occur. In contrast, this occurred in the use of $TiCl_4$ or $TiOCl_3$ [115].

The calcination process or sintering temperature of polyoxocation-intercalated clay is a crucial factor, mainly for the formation of the metal oxide nanoparticles phase. The formation of the metal oxide phase during the sintering process is thermodynamically controlled by thermal change, including the set temperature and heating rate. Along with the increasing particle size, clay destruction may occur due to the rapid heating rate, which is directly expressed by the reduced specific surface area. The pillaring of hectorite and montmorillonite with ZnO demonstrated these variable synthesis outcomes [116,117]. Comparing the formation of metal oxide phase in pillared clay form with the formation of

pure metal oxide nanoparticles is a better approach. As an example, the formation of ZnO nanoparticles is governed by the sintering temperature. As a photocatalyst, the wurtzite phase can be achieved at a temperature of 700 °C, which also affects the morphology of the nanoparticles [116]. Particularly for TiO_2, the increasing temperature tends to produce a rutile phase instead of an anatase phase, which expresses less band gap energy. This considerably influences the optical properties of the material [118]. As an example, the varied temperature from 300 to 800 °C, and revealed the optimum anatase:rutile ratio at a temperature of 500 °C.

For specific applications, the combination of two metal oxide pillars was also synthesized. For example, in order to provide photoactivity with a high specific surface area of the nanocomposite, a combination of Al_2O_3 and Fe_2O_3 was established. The aluminum pillarization of clay is well-known to result in an increased specific surface area due to the stability of polyoxocation of the Al_{13} Keggin ion; moreover, the photocatalytically active Fe_2O_3 in a homogeneously distributed form contributes as a photoactive material. Similarly, combinations of Cu/Al-, Zn/Al-, and Cr/Al-pillared clays have been reported. Cu/Al-pillared clay was prepared as a combination of intercalated poly(hydroxy)aluminum ($Al_3(OH)_4^{5+}$) and copper $Cu_3(OH)_4^{2+}$ species, using slow titration to produce $AlCl_3$ and $CuCl_2$. The molar ratio of $Cu^{2+}:(Al^{3+}+Cu^{2+})$ in the precursor solution affected the increasing d_{001} and specific surface area [119]; the optimum synthesis conditions were a Cu:(Al+Cu) molar ratio of 0.1:1 and OH:Al = 2.5:1 [120]. Those ratios determined the characteristics of the material, which play an important role in the electrocatalytic degradation of CO_2 as well as oxidative features in CWPO.

Studies on the combination of the mixed metal pillarization of Al/Fe-pillared clays revealed the specific contributing properties of each metal for such catalytic activity. Based on a solid state study using ESR and 27Al-NMR spectroscopy, mixed pillars exhibiting a Keggin-like formula $[FeAl_{12}O_4(OH)_{24}(H_2O)_{12}]^{7+}$ ($FeAl_{12}^{7+}$) were utilized as active species in the pillaring process [121]. Table 2 provides some crucial factors for the synthesis of pillared clay.

From the schematic representation of clay pillarization, the increasing basal spacing, d_{001}, is an important earmark for the success of pillarization, which influences the surface morphology. Figure 7 shows the increasing d_{001} features from Fe_2O_3-pillarization to bentonite identified by XRD and SEM analyses [123]. The shift in d_{001} reflection to lower angle indicated the enhanced interlayer space, from 14.9 nm in the bentonite sample (Bent) to 15.45 nm and 16.78 nm for Fe_2O_3-pillared bentonites with Fe contents of 5 mmol/10 g and 10 mmol/10 g (Fe/Bent-5 and Fe/Bent-10), respectively. This is also reflected by the evolution of the surface morphology of the sample to be flakier in structure, as indicated by the immobilized Fe_2O_3. Similar patterns of XRD and SEM results were reported for TiO_2, ZnO, and other metal oxides [113,137]. The change in interlayer space could also be confirmed by TEM analysis, in which an example from SnO_2 pillarization is presented in Figure 8. In addition, at the high concentration of metal oxide, such dispersed nanoparticles are identified beside the fringes correlated with the d_{001} of the clay structure (Figure 8a,b) [138,139].

When using natural clay, the mineral composition strongly influences the characteristics of the pillared clay. A composition of smectite and illite, and the presence of a non-swellable mineral, such as quartz in the material, has the effect of decreasing the capability of clay to be intercalated with the polyoxocation of the precursor [127]. Pretreatments, including the demineralization of impurities through the addition of hydrogen peroxide, as well as refluxing the minerals in acid, were reported to be effective to increase the basal spacing, d_{001}, of clay, along with the increased specific surface area [140–142]. Intensive studies on the effects of initial clay were also carried out for the synthesis of porous clay heterostructure [143].

Table 2. Some pillared clays syntheses and highlighted crucial factors for the syntheses.

Pillared Clay	Precursor	d_{001} (nm)	Crucial Factor	Ref
Fe_2O_3-rectorite	Na_2CO_3 solution in mixture with $Fe(NO_3)_3$ at the molar ratio Na:Fe of 1:1, under stirring at 25 °C	0.25	-	[79]
TiO_2/montmorillonite	Tetrabutyl titanate in mixture with HCl by slowly dropping 0.5 of [Ti]:[H^+] molar ratio under stirring 1.0 h	0.357	Calcination temperature determined the specific surface area	[113]
TiO_2/montmorillonite	Various pillaring precursor: Ti-PILCs consist of adding $TiCl_4$ to a solution of HCl, which can be diluted with deionized water under vigorous stirring to obtain hydrolyzed Ti^{4+}	0.2–0.3	HCl:Ti molar ratio; temperature at which the pillaring solution is prepared; clay suspension concentration; mmol of Ti:clay ratio; and calcination temperature	[122]
Fe_2O_3-pillared bentonite	$FeCl_3$ and NaOH at a molar ratio $^-$OH:Fe = 1:1, stirred at room temperature overnight	0.06–0.84	Fe molar-to-mass ratio influencing the specific surface area and basal spacing d_{001}	[123]
Fe_2O_3-pillared montmorillonite	Trinuclear acetate Fe(III) ion, [$Fe_3(OCOCH_3)_7OH \cdot 2H_2O$]	0.1	Fe molar-to-mass ratio influencing the specific surface area	[111]
Fe_2O_3-pillared montmorillonite	$FeCl_3$ and NaOH at the molar ratio $^-$OH:Fe = 1:1, stirring for 4 h at room temperature	-	$^-$OH:Fe molar ratio, Fe content and calcination temperature are the important parameters influencing the character of pillared clay	[124]
SnO_2/montmorillonite	Slowly titrated with NaOH and $SnCl_2$ solution with Sn:OH molar ratio of 1:1, stirred overnight	1.4–1.6 nm	Sn molar-to-mass ratio influencing the specific surface area, basal spacing d001, and particle size of SnO_2	[125]
Cu/Al-pillared bentonite	Cu^{2+}/(Al^{3+}+Cu^{2+}) molar ratios 0, 0.05, 0.1, 0.15 and 0.2.	0.7–0.88	Cu^{2+}/(Al^{3+}+Cu^{2+}) molar ratios determined the increasing d_{001} and specific surface area	[119]
TiO_2-pillared montmorillonite	The mixture of HCl-Ti isopropoxide at the HCl:Ti molar ratio of 10		The calcination by microwave irradiation influenced by the power of microwave	[126]
Al/Fe-pillared clay	$AlCl_3$ in mixture with $FeCl_3$ titrated with NaOH		The starting clay	[127]
Al/Fe-pillared clay	$AlCl_3$ in mixture with $FeCl_3$ titrated with NaOH	0.45	Al:Fe molar ratio influenced the physicochemical character of material	[128]
SnO_2/montmorillonite	$SnCl_2$ in mixture with NaOH at the Sn:OH molar ratio of 1:1		Sn:montmorillonite mass ratio influenced the character of materials	[80]
TiO_2-pillared montmorillonite	Titanium isopropoxide-HCl	0.25	Microwave power influenced the physicochemical character of material	[129]
Al-Fe pillared clay	$FeCl_3$ and $AlCl_3$ with the molar ratio of Al:Fe = 5:1, titrated with NaOH under vigorous stirring to obtain a molar ratio of OH:(Al+Fe) = 2	0.46	Al:Fe and OH:(Al+Fe) = 2 determining the basal spacing d_{001} and specific surface area	[130]
ZnO/sepiolite heterostructure	Zn-acetate and KOH in methanol under precipitation method	Not reported	Material has capability to be support for Fe_2O_3	[131]
SnO_2/bentonite	$SnCl_2$ at various contents (10, 20, and 30 wt.%) in mixture with NaOH at the pH of 11–12, stirred at 60 °C	Not reported	Material has the capability to effectively degrade MB	[132]
TiO_2/sepiolite	Tetrabutyl titanate (TBT) and acetic acid under solvothermal	Not reported	Material has the capability to effectively degrade MB	[133]
TiO_2/montmorillonite	Titanium tetraisopropoxide was added to a vigorously stirred acetic acid solution of 80 wt.%. The resulting white slurry was stirred at 323 K to give a clear TiO_2 sol	0.48	Kind of clay determined the hydrophobicity of pillared clay	[134]
TiO_2/montmorillonite	$TiCl_4$ was diluted with CH_2Cl_2 to obtain a clear solution. Then, the mixture was slowly added to Na–M suspension under vigorous stirring at 65 °C for 4 h under reflex system	1.60	The Ti content in TiO_2–M was 48.6 wt.% with an anatase crystallite size of about 15–20 nm	[135]
ZrO_2/bentonite	A zirconium polycation solution was prepared by the slow titration of a $ZrCl_4$ solution (0.1 M) with a solution of NaOH (0.2 M) under vigorous stirring, using an OH:Zr molar ratio equal to 4:1.	0.95	Ageing temperature of intercalated bentonite influences the distribution of polyoxocations	[136]
TiO_2/montmorillonite	Titanium polycation solution was prepared by the hydrolysis of $TiCl_4$	0.20	Hydrothermal treatment and calcination temperature influenced the increasing d_{001} and titanium dioxide phase	[118]

The metal-to-clay ratio determines much of the catalytic and photocatalytic activity, governing the physicochemical character of pillared clay. From many studies, such as research on the synthesis of TiO_2-pillared montmorillonite and SnO_2-pillared montmorillonite, it can be concluded that the metal-to-clay ratio is not linearly correlated with increasing either the physical characteristics or the catalytic performance of the pillared clay, but it has an optimum condition, which depends on the electronic properties of the surface, the cation exchange capacity of clay, and the affinity of metal polyoxocations to

enter the intercalating region [80,144]. Figure 9 presents the effect of the metal:clay ratio on the d_{001} of pillared clays, indicating the optimum conditions.
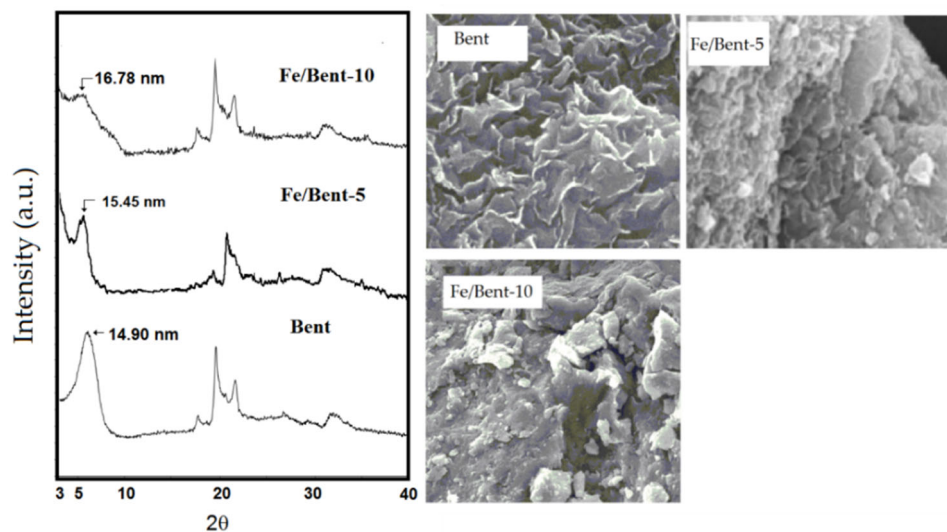
Figure 7. XRD patterns and SEM images of Fe-pillared bentonite with varied Fe content (5 and 10 mmol/10 g). Adapted from Ref. [123] with permission from BCREC Group.
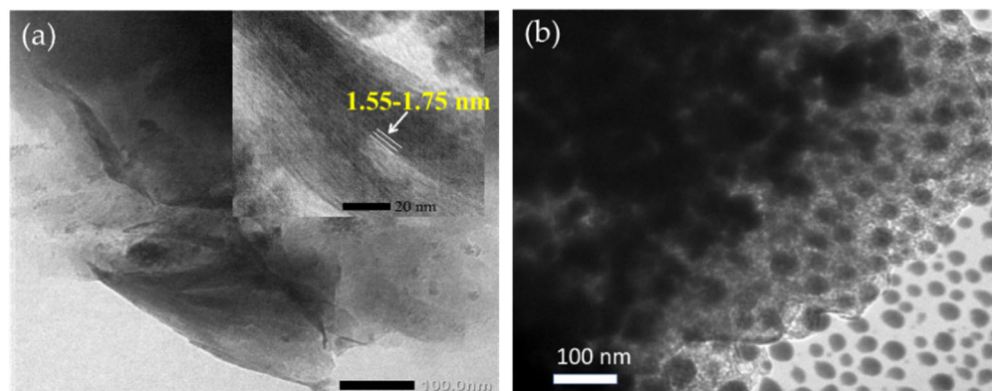
Figure 8. TEM images of SnO_2/montmorillonite at Sn/montmorillonite ratios of (**a**) 2.5 and (**b**) 10.0 mmol/10 g. Adapted from Ref. [80] with permission from the Elsevier B.V., 2021.
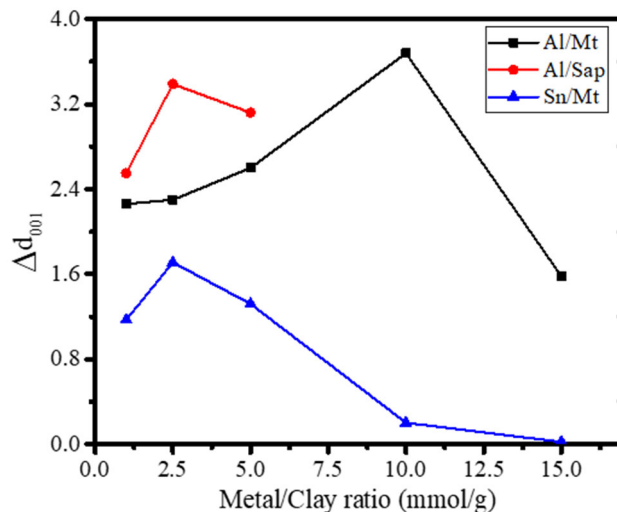
Figure 9. The effect of the metal:clay ratio on the Δd_{001} of pillared clays.

Figure 9 demonstrates that the metal:clay ratio for different metals and clay minerals has an optimum condition to increase d_{001}, as identified for the created porous structure and facilitating the specific surface area.

The change in clay structure by metal oxide pillarization is not only related to surface parameters including the specific surface area and morphology, but is also reflected by the change in the electronic properties of the metal oxide. The higher band gap energy of TiO_2 in the pillared saponite (3.25 eV) compared with the band gap energy of TiO_2 (3.20 eV) was found to correspond to the smaller TiO_2 particle size in the nanocomposite form [145,146]. This is characteristic for the homogeneous distribution of the metal oxide. In addition, the opposite phenomenon of the lower band gap energy occurs, as related to the possible crystal defects. This trend was demonstrated by SnO_2 pillarization into montmorillonite. The band gap energies of SnO_2-pillared montmorillonite are within the range of 2.49–3.18 eV, depending on the Sn content, and are lower than that of bulk SnO_2 (3.6 eV). Oxide formation in the interlayer region is not as simple as that in the bulk form; therefore, the defects in the crystalline system cause changes in the electronic structure of SnO_2 [80].

In addition to clay pillarization with mixed metals, combined metal/metal oxide dispersion into the clay structure can also be conducted, utilizing single-metal-oxide-pillared clay as a support for another metal or metal oxide nanoparticles. This scheme takes two steps: pillarization, followed by an impregnation procedure, as described in Figure 10.
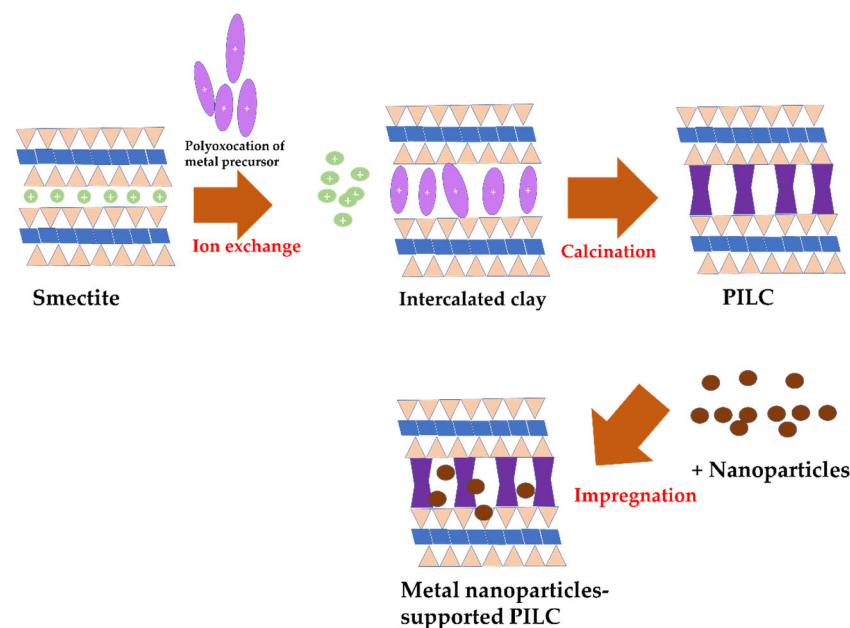
Figure 10. Schematic representation of metal nanoparticle impregnation onto PILC.

Combinations such as TiO_2-impregnated Fe-pillared clay (TiO_2/Fe-PILC), Fe-impregnated Co-pillared clay (Fe/Co-PILC), Ru-impregnated Ti-pillared clay (Zn/Fe-PILC), and Co/Al-PILC exhibited hybrid properties for gaining either homogeneous dispersion or material stability, which are sufficiently accommodating for surface interactions for the catalytic process [147–150]. The immobilized Co^{2+} and Sn^{2+} have been proven as successful catalysts for dye oxidation. On tartrazine oxidation using oxone, Co/Al-PILC was demonstrated to be a stable and efficient catalyst in the degradation of both tartrazine and the detected products [150].

The homogeneous expansion of the clay layers depends on the distribution of polyoxocations during the intercalation step, and dihydroxylation during calcination. Studies of the synthesis of ZrO_2/bentonite demonstrated that the homogeneous clay layers were a function of the diffusion of ions in the interlamellar space. The most effective polyoxocation in the synthesis was in the form of hydroxycation $[Zr_4OH_8 (H_2O)_{16}]^{8+}$, which

rapidly polymerizes by the mixture of $ZrCl_4$ and NaOH at an OH:Zr ratio of 4:1. The order of polymer species which determines the intercalating layers changed as the ageing temperatures changed. From varied ageing temperatures between 25 and 100 °C, it was found that different species sizes caused the irregular stacking of clay layers, and the optimum temperature was 40 °C. The amorphous condition was obtained at 100 °C [136]. Furthermore, the calcination temperature is a meaningful variable for determining not only the homogeneity of metal oxide dispersion, but also the metal oxide phase [124]. In the synthesis of pillared clays, the distance between the sheets of clay structure results from the dehydration and dehydroxylation of intercalated metal polyoxocations along with the formation of metal oxide as permanently linked adjacent layers. Therefore, the optimization of dihydroxylation temperature for such intercalated cations is a crucial step.
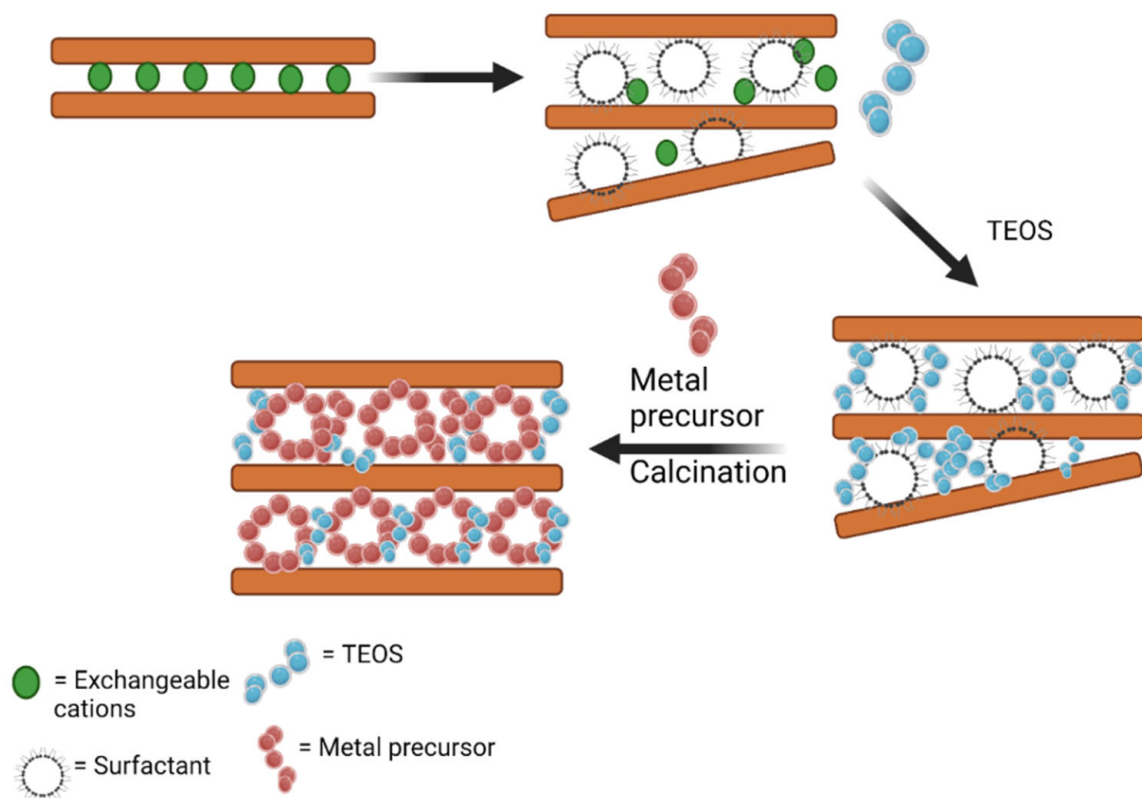
5.3. Porous Clay Heterostructure

The creation of a mesoporous structure can also proceed through the combination of cationic precursors incorporated with silica or titania pillars, known as a porous clay heterostructure (PCH). The higher interlayer distance of the basal spacing of clay structure within the range of 3.02–3.49 nm is obtained with templating agents, such as cetyl trimethyl ammonium or other organic compounds, to form a bigger space for positioning the metal oxide arrangement, as can be observed in Figure 11. From several studies, it was found that the deposition of metal oxide within the PCH structure produced well-dispersed forms [151]. The increasing basal spacing, d_{001}, was within the range of 0.1–3.0 nm, and could be obtained by clay pillarization which depends on some crucial factors in the synthesis such as the stability of polyoxocations, pH of the intercalation, calcination temperature, and metal content. Surface modification using a surfactant prior to polyoxocation intercalation facilitates the assembly of nanoparticle formations of the metal via controlling agglomeration and directing the homogeneous dispersion of the metal. The larger pore opening related to the molecular size of the organic compound is a crucial factor for the creation of porous structures [131,134]. The organic matter from the surfactant was removed by thermal treatment at 500 °C. A significantly increasing specific surface area was also reported by dispersed ZnO in the PCH formation from saponite, in comparison with the ZnO/pillared saponite [152]. With the same amount of Zn (10 mmol/g), ZnO-pillared saponite exhibited a specific surface area of 188 m^2/g; meanwhile, ZnO/PCH showed 770 m^2/g. Similar phenomena were also reported in the PCH synthesis of $ZnO-TiO_2$/delaminated montmorillonite in comparison with the pillared form [153]. The increasing porosity brings increased thermal stability for some PCHs. For example, in the synthesis of the porous structure of titania/silica-montmorillonite [151], it was found that the silica–titania clusters were formed by separated tetracoordinated titanium cations incorporated into the silica pillars. The cluster formation was found to be enhanced, demonstrating thermal stability at temperatures exceeding 600 °C.

It can be seen from Table 2 that the physicochemical characteristics of pillared clays are mainly governed by either the molar ratio of metal-to-base, or the metal-to-total-metal in the pillaring precursor, in addition to the ratio of metal-to-clay-mass [80]. Studies on the effect of the Sn-to-montmorillonite mass ratio described the presence of an optimum point for increasing the basal spacing and specific surface area of montmorillonite.

5.4. Clay Modification with Metal Nanoparticles

The dispersion of metal nanoparticles into the clay structure can be conducted by either an ion exchange process of the metal ions with native cations of the clay mineral, or the in situ dispersion of metal nanoparticles into the clay structure. The dispersion of nanosized zero valent irons (ZVIs) into montmorillonite structure by the ion exchange method was conducted, resulting in homogeneously distributed nanoparticles [154]. After the ion exchange process had reached surface equilibrium, the mild reduction of inserted Fe^{2+} was achieved with $NaBH_4$. Similarly, the dispersion of Cu nanoparticles into montmorillonite was conducted by exchanging cations with $CuCl_2 \cdot 2H_2O$ with consideration of the cation

exchange capacity, followed by reducing exchanged Cu^{2+} with hydrazine to form Cu nanoparticles (Cu NPs) [155]. The same scheme was also performed for the dispersion of Ni NPs in montmorillonite [156] and Pd NPs [157]. The in situ metal nanoparticle dispersion was actually similar to the ion-exchange method, but the certain amount of metal was chosen without consideration of cationic equilibrium [158–160]. The dispersion of Au NPs into attapulgite is an example where Au NPs are prepared by the most commonly published method—Frens. The reduction of Au from a $HAuCl_2$ precursor with citric acid was conducted prior to dispersion with attapulgite [161] and montmorillonite [162]. The ultrasound-assisted dispersion of colloidal Au NPs into montmorillonite was proposed as a technique to yield homogeneous dispersion [163].

Figure 11. Schematic representation of porous clay heterostructure synthesis.

The impregnation of green synthesized nanoparticles is a novel method reported by several recent papers. Metal nanoparticles are prepared by mixing precursor salt with a plant extract at a certain volume ratio and reaction condition to produce the nanoparticle solution. The solution is then dispersed into clay suspension to produce the nanocomposite. The greenness of using plant extract as a bio-reductor as a replacement for common reductors such as $NaBH_4$ and other corrosive chemicals is the main consideration for the popularity of this method [158,164]. In addition to the reductor for NPs formation, the secondary metabolites from the plant extracts play roles in maintaining the stability of the nanoparticles. Some examples from this scheme are kaolinite-supported bio-fabricated Ag NPs using *Murraya koenigii* fruit extract [165], montmorillonite-supported *Urtica dioica* leaf-extract-mediated Ag NPs [165], and montmorillonite-supported Ag NPs fabricated using *Ocimum basilicum* L. and *Teucrium Polium* L. [166]. Montmorillonite-supported Ni NPs were also prepared through a similar scheme [167]. Figure 12 is a schematic representation of the synthesis method.
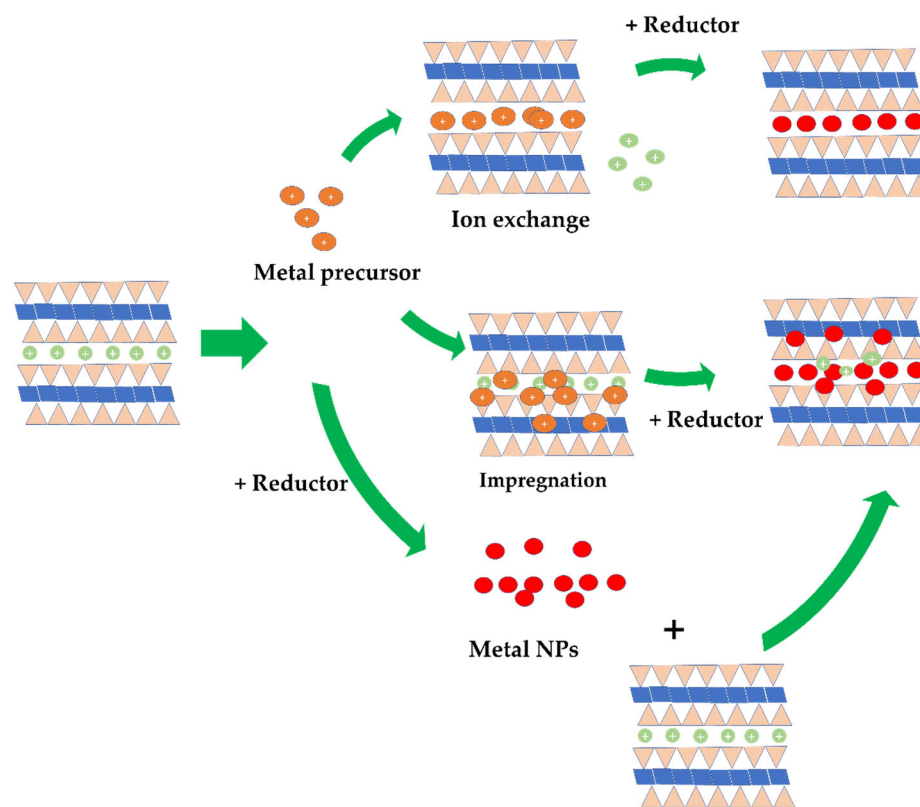
Figure 12. Schematic representation of the dispersion of metal nanoparticles in clay structure.

In addition to their excellent activity as antibacterial agents, clay-supported Ag NPs were established as versatile catalysts for the degradation of nitroaryl (4-nitrophenol) and methylene-blue-containing solution [168,169]. Ni NPs/montmorillonite presented excellent catalytic activity in the oxidation of methanol [167].

The applicability of modified clay for industrial applications is a crucial issue. The scaling-up process of modified clay preparation faces challenges mainly related to intercalation, washing, and drying steps [56,170]. Minimizing water use in the synthesis was attempted through utilizing high concentrations of clay suspension in the intercalating metal oxide precursor and optimizing water for neutralization/washing [171]. A successful scaling-up study was reported for Al/Fe-pillared clay synthesis by a factor of 1000, from the lab (10 g) to the pilot scale (10 kg) [172]. Referring to the complexity of attaining optimum conditions in other metal oxide pillared clays, optimization for scaling-up is an important aspect for development.

5.5. Intensification on Metal/Metal Oxide-Supported Clay Nanocomposite

Referring to the green chemistry principles and applicability for industrial scaling-up, minimizing energy and time required for the synthesis of clay-based nanocomposites is under consideration. In this regard, intensification procedures for the intercalation step have been widely reported. Several techniques are detailed subsequently.

5.5.1. Mechanochemical

The mechanochemical synthesis of nanocomposites involves a high-energy milling technique and is usually carried out at controlled pressure. The intercalation of metal/metal oxide into the clay structure can be achieved with this method. For example, Li et al. (2020) synthesized a ternary polyethyleneimine clay nanocomposites using a mechanochemical technique for the removal of heavy metal pollutants in wastewater [173]. Mechanochemical techniques can produce different physicochemical properties of materials, such as changing the particle/crystal size, changing the lattice structure, changing the morphology,

increasing the surface area, and even generating structure defects. Therefore, this technique is quite effective for the intercalation process on clay structures, because physically, the clay structure will undergo a rearrangement that enables easy modification and intercalation. However, this method also has several disadvantages: (1) the small nanoparticles formed have low homogeneity, meaning that the particle size cannot be appropriately controlled; and (2) contamination from the grinding material causes a lower purity of the nanocomposite material.

This mechanochemical method has been widely used to synthesize metal/metal oxide intercalated in clay. In this method, nanocomposites can be prepared by direct mixing of the constituent materials. Here, several important factors that determine the characteristics of the resulting nanocomposite are the purity of the raw material, the type of raw material, the distribution and size of the resulting particles, and the degree of agglomeration in the process [174]. Contamination of the grinding medium can be avoided by using appropriate materials such as zirconia, alumina, silicon, and tungsten carbide. Yang et al. (2021) prepared zero-valent aluminum (ZVAl)-clay nanocomposites using ball milling with agate balls [175]. The modification of ZVAl-clay showed excellent degradation for 4-chlorophenol with an improved efficiency of around 38.7%. This method is more suitable for synthesizing composites derived from raw materials such as powders. Although this method is highly suitable for the preparation of various nanocomposites and in intercalation processes, the main drawback of this method is the low particle size homogeneity.

5.5.2. Microwave Irradiation

The synthesis of metal/metal-oxide-pillared clay nanocomposites has been widely reported and optimized for producing excellent chemical activity properties. Foroughi et al. (2017) synthesized CdO/clay nanocomposites via simple microwave irradiation [176]. Their study found that different microwave powers could produce different particle sizes and morphologies of final nanocomposite materials, from sheet to rod nanostructures. In chemical syntheses, microwave irradiation can provide thermal and non-thermal effects. Thermal effects of the irradiation process can result in polarization of the molecule without the formation of bonds or the generation of new chemical groups within the molecule itself. This phenomenon increases the material temperature and reaction rate during the synthesis process. In addition, microwave frequencies can stimulate molecules' vibrations or rotation, resulting in energy level transitions, even to a more active excited state, thereby changing the activation energy (E_a) and the reaction rate [177].

The microwave method is commonly used to intercalate metal/metal oxides into the clay structure because it requires a short time for the synthesis process (less than 15 min). Barakan and Aghazadeh (2016) prepared Al- and Fe-pillared nano-bentonite via microwave irradiation for 3 and 7 min using highly pure aluminum salt ($AlCl_3 \cdot 6H_2O$) and iron salt ($FeCl_3 \cdot 6H_2O$) [178]. In their study, the constant molar ratio of Al^{3+}:Fe^{3+} was intercalated into the clay structure with a short process at 160 W power irradiation. The results showed that the prepared nanocomposite had a small particle size (less than 1 μm) and a high surface area, almost sixfold higher than the unpillared process. However, this method still has several limitations: the synthesis process can only be carried out on a small/limited scale; a complex process for waste treatment is required; inhomogeneous energy distribution; it is difficult to control the temperature; the flammable organic solvent has limited uses; and the heat generated from irradiation cannot effectively penetrate the container reactor, so in some cases, the synthesis is considerably less efficient [179]. Therefore, Hao et al. (2021) developed the combined microwave–hydrothermal synthesis route for producing $Co/CoAl_2O_4$/sepiolite nanocomposites [180]. The material was prepared under alkaline conditions of 1 mol/L NaOH at 240 °C for 3 h, followed by reduction at 650 °C. The composite materials could easily be obtained by these methods with a high efficiency as a cobalt-based catalyst. The combination and modification of these methods have the advantage that the synthesis can be carried out on large scales.
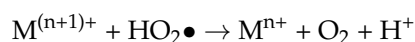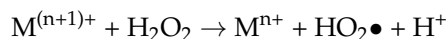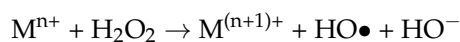
5.5.3. Ultrasound Irradiation

In recent decades, ultrasound irradiation has been widely used as an alternative energy source in the synthesis of clay-based nanocomposites to achieve green and more sustainable chemical-based synthesis. The effect of ultrasonic waves causes molecules to oscillate because the average distance between the molecules increases, which increases the speed of the synthesis reaction process. Unlike microwaves, ultrasonic irradiation requires lower energy requirements, shorter reaction times, and high product purity [181]. Olaya et al. (2009) prepared pillared clay with Al-Fe-Ce and Al-Fe using ultrasound irradiation in a 30 min reaction process [182]. They found that increasing the concentration of Fe in pillared clay changed the morphology and microporous area of the clay materials. Compared with conventional methods, the developed methods can reduce the consumption of water by up to 90%, as well as reduce the processing time and process cost. The addition of an ultrasonic step to the synthesis process did not change the material properties, such as the catalytic activity and the acidity of the pillared clay. However, the pillarization process with this method produced higher particle size homogeneity than the conventional method. The process of metal/metal oxide pillarization into clay using this method can be optimized by considering several factors, such as ultrasonic irradiation power and viscosity [183]. This method can be used for natural clay pillarization processes by the mixing pillar solution with a clay suspension, using less water and reacting faster. Ultrasound irradiation (20 kHz–10 MHz) from a liquid suspension can cause an acoustic cavitation effect. This process involves generating, growing, and collapsing bubbles in a liquid medium and causes extreme transient conditions, such as pressure in the system in the range of ~500 atm and a high temperature of ~5000 K. Changes in conditions can cause shockwaves induced by cavitation, which trigger the formation of nanostructures [184].

6. Clay-Supported Metal Oxide in AOPs

Clay-supported metals and metal oxide nanoparticles could act as catalysts in processes of catalytic oxidation (CO), catalytic wet peroxidation (CWPO), catalytic ozonation, as well as photocatalysts in photocatalytic oxidation (PCPO) and peroxidation (PCO) reactions. Table 3 presents some research on the synthesis and applications of clay-supported metal and metal oxides for AOPs along with the highlighted performances of their activity.

Catalytic oxidation reactions are based on the catalytic generation of hydroxy radicals in mild conditions, which refers to the high oxidation potential of HO•. More specifically, catalytic wet peroxidation utilizes hydrogen peroxide decomposition by transition metallic cations (M). The catalyst is oxidized by H_2O_2, generating HO•, and with additional H_2O_2 molecules it will generate hydroperoxyl radicals (HO_2•), according to the following equations:

$$M^{n+} + H_2O_2 \rightarrow M^{(n+1)+} + HO\bullet + HO^-$$

$$M^{(n+1)+} + H_2O_2 \rightarrow M^{n+} + HO_2\bullet + H^+$$

$$M^{(n+1)+} + HO_2\bullet \rightarrow M^{n+} + O_2 + H^+$$

In the mechanism discovered by H.J.H. Fenton at the end of the 19th century, highly oxidative properties of hydrogen peroxide were observed in the presence of iron ions during the oxidation of tartaric acid. Thus, the homogeneous Fenton process was developed. The drawbacks of the process are related to the maximum oxidation/degradation efficiency (DE), which could only be achieved in a narrow pH interval (2–4), in addition to non-recoverable metal ions. Forming metals and metal oxides into a stable chemical support demonstrated the feasibility of overcoming these problems.

Metal and transition metal elements are capable of undergoing this redox reaction due to their oxidation states, which raises the possibility of repetitive oxidation–reduction. A variety of metal and metal oxide catalysts can be utilized as active catalysts, including Fe, Fe_2O_3, Fe_3O_4, Co, Cu, CuO, ZnO, and ZrO_2; their immobilization on various solid supports, such as carbon, graphene, zeolite, and clay minerals, has also been reported.

Referring to the data in Table 2, the enhanced oxidation rate and degradation efficiency of the CWPO was conclusively obtained by utilizing clay-supported metal and metal oxide.

The most commonly used metal in Fenton, photo-Fenton, and photo-Fenton-like processes is iron oxide. Its immobilization on clay minerals has been intensively studied for many pollutant compounds consisting of dyes, pesticides, and other persistent organic compounds [102,185,186]. Fe_2O_3/montmorillonite prepared in some studies exhibited enhanced catalytic and photocatalytic activity. The increased activity is related to more oxygen vacancies in its pillared form compared with Fe_2O_3 nanoparticles (nFe_2O_3), which are capable of inducing increased reactive oxygen species (ROS) generation in the presence of a light source. It was reported that the photo-assisted degradation of diethyl phthalate (DEP) was increased by 2.5-fold as compared with nFe_2O_3. The surface-bound $\bullet OH$ was the main radical playing a role in the degradation mechanism, and it can be suppressed by the presence of competitor anions such as Cl^-, NO_3^-, and CO_3^{2-}, as well as the pH condition of the solution. The stabilized iron oxide was found to enhance the effectiveness, with insignificant changes in photocatalytic and catalytic activity after three cycles [186]. The homogeneous distribution of the metal oxide on the surface morphology affects the reaction effectiveness, which is also controllable by the dispersion method. As an example, in the synthesis of nano-Fe_2O_3/montmorillonite, the impregnation method yielded a different distribution of the nanoparticles as compared with the coprecipitation method [187]. The increasing specific surface area of montmorillonite from 17 to 62 m^2/g was related to the changed basal spacing (d_{001}).

Minimizing iron leaching during the treatment was another aim of combining Fe with other metals such as Co, Cu, Zn, and Zr. The highly stable catalyst in a wider pH range was attained with Fe/Co-pillared clay with minimal leached iron identified at the end of the reaction: lower than 0.1 mg L^{-1} [148]. In the case of MnO_2-supported clay, α-MnO_2 is the dominant phase identified to be inserted into the clay structures, either for montmorillonite or saponite [99,122,188]. The characteristics of high oxidation potential and surface activity of the hydroxyl structure of the phase strongly support the oxidation mechanism. This revealed the rapid and complete oxidation of MB at room temperature without any oxidant [99].

Montmorillonite-supported Cu nanoparticles exhibited high degradation efficiency in the CWPO of methylene blue (MB) (95.9%); additionally, clay surface pre-modification with ρ-amino benzoic acid before the nanoparticle support was formed progressively resulted in the complete removal of MB [155]. In this case, immobilizing Cu NPs reduced the surface potential and caused a dramatic fall in the surface area and total pore volume, due to the rupture of the microporous structure. The homogeneously distributed Cu NPs, 8 nm in size in the montmorillonite matrix, represented the effective role of Cu NPs for surface interactions and inducing the oxidation mechanism. Similarly, the supportive adsorption interaction was identified from the CWPO of atrazine using montmorillonite-supported Cu NPs. Mechanistic studies of adsorption and oxidation have revealed the contribution of atrazine adsorption by Cu as an active catalyst via coordination bonding with nitrogen from the atrazine structure, yielding a significant reduction in the chemical oxygen demand of the treated solution. Cu_2O and CuO identified on the surface are recognized as the redox-active species within the pores, layers, and outside of the montmorillonite surfaces [189]. In an ionic form, Cu^{2+}-immobilized aluminum-pillared montmorillonite (Cu/Al-PILM) showed a capability for use in Fenton and photo-Fenton treatments of RO16 [190]. A slit-like mesopore structure with pore diameter of 3.3–3.8 nm and ~6–35 nm was observed in Cu/Al-PILM, with an increasing trend in mesoporosity with the increasingly impregnated Cu^{2+} concentrations.

The oxide form of CuO nanoparticles not only occupied the interior interlayers, but also the exterior surfaces of Cu/Al-PILM. The mesoporous form significantly contributed to effective heterogeneous catalysis for the removal of RO16. Even though many studies have revealed that clay-supported Cu NPs of CuO expressed stability, the combination of Cu with other metals, such as Fe and Al, in mixed-metal-pillared clay contributed towards
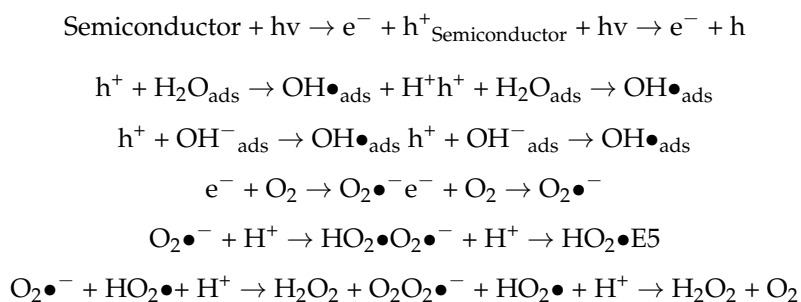
resulting in better catalytic properties. The appreciable catalytic activity was reported by the combination of such metal pillaring species with iron, such as Al-Fe-pillared clay or Cu-Fe-pillared clay [128,130].

The use of combined metals represented the more effective electron–hole pair oxidation/reduction mechanism. The increasing effectiveness of Zr-immobilized pillared clay in a wastewater model was reported from Zr-Cu/Al-pillared clay for treating wastewater from a winery. The significant improvement in total organic content (TOC) removal from 46% to 60% was exhibited as a synergetic effect of both Zr and Cu on the photocatalytic degradation process. The greater band gap of Zr (5.8–7.1 eV) supported the generation of electron–hole pairs, which migrate to the photocatalyst surface and yield radical species that can react with organic molecules upon redox reactions. The electron transfer process is enhanced by the successive redox of Cu^{2+}, a transition metal which continuously releases e-species, induced by the presence of a permanent irradiation source (UV-C). However, starting clay is still the important factor to be considered in the synthesis. The cation exchange capacity, pore structure, and specific surface area strongly determine the capability in the cation exchange process. This considerably affects the final structure of the material as well as the redox activity and stability in the reaction medium [127].

Mixed-metal-oxide-pillared clays have been prepared in various compositions and metal sources. One such example is Al/Zr-pillared montmorillonite [191]. An Al:Zr molar ratio of 3:1 was found to be the most active catalyst for the CWPO to phenol. The catalytic activity was strongly influenced by pH, because the zeta potential of the catalyst surface influenced the interaction between the target molecule and the catalyst. The high permanent negative charge on the basal surface of raw clay particles might arise from the high degree of isomorphous substitution of structural Si^{4+} in the tetrahedral layer by polyoxocations from the pillaring agents. This leads to changes in the surface charge arising from the hydroxyl groups at the edges of the parent clay particles. Resulting from the Lewis acidity of the metal precursor, the pillared clays usually have higher zeta potentials than the parent clay [191]. This phenomenon is also reflected in metal-oxide-pillared clay for the PCPO process. Similarly with AOPs utilizing unsupported metal and metal oxides, some influencing parameters, such as pH, oxidant dose, catalyst dose, temperature, target molecule, and reaction time, strongly affect the efficiency of the process. A study on Fe_2O_3/montmorillonite for phenol degradation revealed the pH to be the critical factor for influencing the degradation efficiency of phenol removal.

Particularly for photocatalytic oxidation, only the severe metal oxide of semiconductor photocatalysts can be utilized. The basic principle of photocatalysis relies on the generation of electrons and holes as the semiconductor is impinged by photons. In addition, the redox potential of a donor species on the surface of the photocatalyst needs to be more negative (higher in energy) than the valence band position of the semiconductor to fill the electron vacancies. Similarly, acceptor molecules must have a more positive redox potential (lower in energy) than the conduction band. Figure 13 presents the redox potential diagram.

As an electron is excited from the valence band to the conductance band, •OH radical will be produced from the interaction between H_2O and the solvent, which then undergoes propagation and complete oxidation of the target molecule in the treated solution. The oxidation mechanism can be summarized by the following equations:

$$\text{Semiconductor} + h\nu \rightarrow e^- + h^+{}_{\text{Semiconductor}} + h\nu \rightarrow e^- + h$$

$$h^+ + H_2O_{ads} \rightarrow OH\bullet_{ads} + H^+ h^+ + H_2O_{ads} \rightarrow OH\bullet_{ads}$$

$$h^+ + OH^-{}_{ads} \rightarrow OH\bullet_{ads}\ h^+ + OH^-{}_{ads} \rightarrow OH\bullet_{ads}$$

$$e^- + O_2 \rightarrow O_2\bullet^-\ e^- + O_2 \rightarrow O_2\bullet^-$$

$$O_2\bullet^- + H^+ \rightarrow HO_2\bullet O_2\bullet^- + H^+ \rightarrow HO_2\bullet\ \text{E5}$$

$$O_2\bullet^- + HO_2\bullet + H^+ \rightarrow H_2O_2 + O_2 O_2\bullet^- + HO_2\bullet + H^+ \rightarrow H_2O_2 + O_2$$
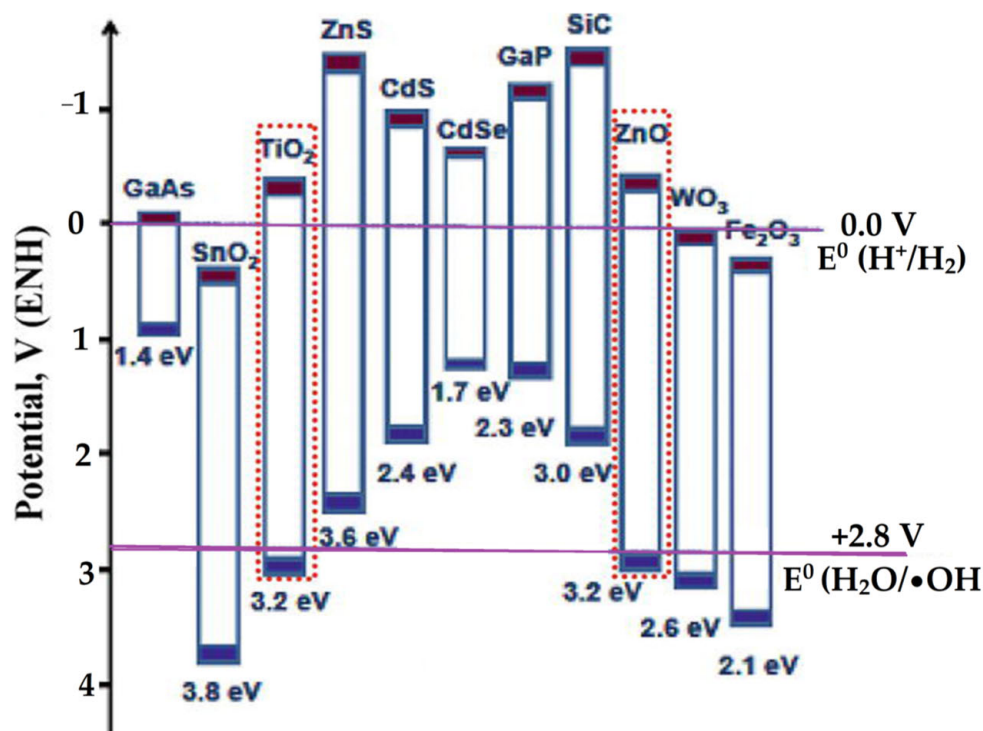
Figure 13. Potential diagram of some semiconductors.

Enhanced photocatalytic efficiency can be achieved by the higher band gap energy of the semiconductor compared with the redox potential of $H_2O/\bullet OH$, as well as the suppressed recombination of electron–hole pairs. The increasing band gap energy, referring to the quantum size effect phenomenon, was reflected by the use of nano-sized metal oxide; moreover, minimizing the recombination can be achieved by trapping the electron or hole in a defect from the conductive support. Sensitization of the metal oxide photocatalyst to overcome the limitations of a narrow-light response range is a strategy for low-cost photocatalysis applicable with sunlight. These strategies were also attempted for clay-supported metal and metal oxide nanoparticles.

TiO_2 is the most popular photocatalyst, as is its clay-supported metal oxide form. Various kinds of clay minerals, such as bentonite, montmorillonite (Mt), kaolinite, hectorite, laponite, halloysite, palygorskite, and attapulgite, have been utilized as TiO_2 supports. The use of such Ti precursors as titanium oxide chloride, titanium tetrachloride, titanium iso-propoxide, and titanium (IV) butoxides were reported either in the pillarization procedure or impregnation procedure. The particle size of assembled TiO_2 nanoparticles on the clay support is determined by several factors, including the morphology and clay mineral's structure. The deposition of TiO_2 anatase in hectorite, an expandable clay mineral, was found to result in important structural changes at the clay mineral surface for enhancing the photocatalytic activity, compared with its incorporation in kaolinite [192]. In more detail, as a determining factor, the dispersion of TiO_2 in a nanoflake kaolinite exhibited a smaller TiO_2 NP size distribution compared with the dispersion in nanorod kaolinite [193]. From various clay-supported-TiO_2, it can be concluded that a higher adsorptive behavior is the highest contributing performance in photocatalytic activity compared with bulk-TiO_2, including Degussa P25. From various dye molecule targets in photocatalytic oxidation experiments, the more significant degradation efficiency on cationic dye rather as opposed to anionic dye was identified. In similar reaction conditions of photocatalytic degradation utilizing TiO_2/montmorillonite, the removal rates were in the order: crystal violet (97.1%) > methylene blue (93.20%) > rhodamine B (79.8%) > methyl orange (36.1%) > Congo red (22.6%) [194]. From the perspective of releasing nanoparticles from the treated solution, montmorillonite plays a role in inhibiting the homo- and hetero-aggregation of TiO_2 NPs.

Depending on the presence of natural organic matter (NOM), pH, and electrolytes, TiO_2-montmorillonite exhibited higher stability [195]. Some experiments on the sensitization and doping of TiO_2/clay as a strategy for enhancing photocatalytic efficiency related to the light range and electron hole recombination have been conducted. The use of a ruthenium complex significantly improved the activation capability of TiO_2/saponite in the visible light region [196]; moreover, the increased band gap energy was achieved by the doping of TiO_2/montmorillonite and TiO_2/Kaolinite with Bi [197], W [153], Fe, and N [198–200]. W-doped TiO_2/montmorillonite demonstrated a removal efficiency of atrazine of about 40% under visible light; however, undoped TiO_2/montmorillonite was almost totally inactive [153]. With the same target molecule of atrazine in a photocatalytic oxidation system, boron-doped TiO_2/montmorillonite demonstrated a fourfold higher rate than the undoped system. The doped nanocomposite exhibited a favorable phase–junction structure in the visible light region, which could potentially be developed in simpler and less expensive photocatalytic systems [201].

The basic photo-Fenton reaction utilized Fe; however, immobilized Fe and its oxide in clay supports demonstrated excellent photocatalytic activity in the PCPO of various target molecules. Using montmorillonite-supported nanosized zero valent iron (ZVI) via an ion-exchange procedure, followed by mild reduction, produced a homogeneously dispersed ZVI with a mean particle size of 0.86 nm. The stability of the dispersed ZVI was acceptable [154]. Additionally studied were montmorillonite-supported Fe_2O_3–Fe_3O_4 NPs (NIOM), which have also shown better reusability compared with Fe_2O_3–Fe_3O_4 NPs. The contribution of the montmorillonite support was critical in decreasing the aggregation and size of the crystals, improving the thermal stability of the crystals. This indicated that the degradation rate of methyl orange when using NIOM was 1.47-fold faster with 45 min of irradiation compared with Fe_2O_3–Fe_3O_4 NPs [202].

The incorporation of Fe and Fe NPs in metal-oxide-pillared clays is another strategy to enhance the surface activity for producing ●OH. The tethering of ferrioxalate in CuO-pillared bentonite has been developed to significantly improve 4-NP photocatalytic oxidation [203]. Ferrioxalate provides an extra source of Fe^{2+} for producing $HO^{\bullet}$, as in the classic Fenton mechanism. The significant effect of the amount of photocatalyst was noticed on the degradation rate.

Zinc oxide nanoparticles are a good alternative to TiO_2, taking into account its environmentally friendly and low-cost features; therefore, research on the dispersion of ZnO in clay supports has also attracted considerable interest. Zinc oxide has good photochemical, catalytic, and optoelectronic features, which are related to its band gap energy of around 3.4 eV and is included as the wide-band gap II–VI semiconductor. The strong contribution of adsorptive properties of the clay support have triggered many attempts to improve the high supporting capacity by creating Zn in a PCH form. A well-ordered ZnO/clay heterostructure was synthesized using hectorite and saponite by utilizing a sol–gel reaction of the precursors [204–207]. Similar attempts for photocatalytic activity enhancements were reported through complex attachment and dopants [206].

From the Fe_2O_3/montmorillonite and SnO_2/montmorillonite syntheses, it was revealed that the metal content in the pillaring precursor is an appreciable and crucial factor in determining the surface profile and the particle size of the dispersed metal oxide [123,125]. A higher amount of Sn in the pillaring precursor determined the increasing particle size, which was then correlated with the band gap energy. Furthermore, some factors for AOPs, such as the initial condition of the pollutant, specific surface area, band gap energy, stability, and the presence of oxidants, should be optimized to achieve the best performance, especially in increasing the lifetime of catalysts and photocatalysts. The stability, recyclability, and reusability of the nanocomposite are also important to consider.

Table 3. Some clay-supported metal or metal oxide nanomaterial for AOPs applications.

Clay-Supported Metal or Metal Oxide Nanomaterial	Target Molecule	Process	Remark	Reference
MnO_2 nanosheet/montmorillonite	MB	CO	MB removal achieved 99.89% at 5 min and the catalyst dose of 0.4 g/L	[99]
MnO_2/montmorillonite	Bisphenol A	CO	Bisphenol A removal was almost 100% after 20 min of treatment	[188]
K-MnO_2/CeO_2/Palygorskite	Phenol	CO	90% of phenol removal for the treatment at 130 °C for 103 min	[208]
Fe/Palygorskite	Phenol	CO	CWPO of MB using Cu NPs/montmorillonite gave complete removal	[208]
Fe_2O_3/montmorillonite	phenol	PCPO	Complete phenol oxidation reached at 90 min	[185]
Fe_2O_3/montmorillonite	Diethyl phthalate	CPO	The material showed stability and reusability with insignificant change of photocatalytic activity until 3 cycles	[186]
Fe_2O_3/montmorillonite	Toluene	CO	Complete toluene oxidation reached at 300 °C	[187]
MnO_2/Al_2O_3-pillared montmorillonite	Acetone	CO	Complete acetone oxidation reached at a temperature of 7500 K	[209]
MnO_2/ZrO_2-pillared montmorillonite	Acetone	CO	40% of acetone oxidation reached at a temperature of 7500 K	[209]
Cu NPs/montmorillonite	Methylene blue (MB)	CWPO	CWPO of MB using Cu NPs/montmorillonite gave complete removal	[155]
Cu NPs/montmorillonite	Atrazine	CWPO	Nanomaterials exhibited adsorption and catalytic oxidation activity for atrazine removal with DE of 82.12% and 85.94%, respectively	[189]
Cu-impregnated Al-pillared montmorillonite	Reactive orange 16 (RO16)	CWPO PCPO	Complete removal of RO16 after 90 min by both AOP mechanisms	[190]
Fe/Co-pillared clay	Paracetamol	CWPO	Optimum condition for completely paracetamol removal was treatment for 6 h, H_2O_2 concentration of 472 mg L^{-1}, catalyst dose of 2.5 g L^{-1}, temperature of 80 °C, and initial pH = 3.5	[190]
Zr-pillared clay	4-nitrophenol	CWPO	Complete removal at 4 h with small amount of H_2O_2 and catalyst loading of 2.5 g/L)	[210]
Al/Zr-pillared clay	Phenol	CWPO	The optimum condition for the CWAO process is a pH of 3, reaction temperature of 100 °C, catalyst dosage of 2 g/L, and oxygen pressure of 10 bar. The reaction obeys the first-order power rate law kinetics model with the apparent activation energy of 21.306 kJ/mol	[191]
Zr immobilized in Cu/Al-pillared clay	Winery wastewater	CWPO	The presence of Zr enhanced the oxidation capability of the catalyst	
Fe- and Cu-immobilized in Zr-pillared clay (Fe/Cu/Zr-APILC)	4-nitrophenol	CWPO	Complete removal after 2 h; the highest TOC removal (65.1% after 8 h) was obtained with Fe/Cu/Zr-APILC	[210]
Co-immobilized AL-pillared clay	Tartrazine	CO	Co^{2+} was impregnated onto aluminum-pillared clay and utilized as tartrazine oxidation via PMS	
Copper-pillared ferrioxalate-modified bentonite (Cu/PBC)	4-nitrophenol	PCPO	Maximum DE of 99.89% was achieved with an excess of H_2O_2, and catalyst loading of 2.0 g/L during 6 min of visible light illumination.	[203]
Al–Fe-pillared clay	4-NP	CWPO	Maximum DE of 99.7% with TOC removal and COD removal of 83.6% and 75%, respectively, attained after 300 min with an excess of H_2O_2 at 50 °C	[130]

Table 3. *Cont.*

Clay-Supported Metal or Metal Oxide Nanomaterial	Target Molecule	Process	Remark	Reference
Al–Cu–Fe-pillared clay	4-NP	CWPO	Maximum DE of 99.7% with TOC removal and COD removal of 63% and 65%, respectively, attained after 300 min with an excess of H_2O_2 at 50 °C	[130]
Al–Cu PILCs	4-NP	CWPO	Maximum DE of 99.7% with TOC removal and COD removal of 60% and 55%, respectively, attained after 300 min with an excess of H_2O_2 at 50 °C	[130]
Al/Fe-, and Al/(Fe–Cu)-bentonite	Methyl orange (MO)	CWPO	The Al/Fe-pillared bentonite attained the complete removal of MO after 1 h of reaction at room temperature	[128]
Cu-doped Fe-pillared Tunisian clay (Cu/Fe–PILC)	Phenol	PCPO	Cu/Fe–PILC demonstrated stability for a wide range of pH, from 3 to 7, for the PCPO process of phenol removal. Nanocomposite showed reusability with negligible metal leaching without a noticeable loss of activity	[211]
Fe-pillared clay (Fe-PILC)	Phenol	PCPO	Phenol removal efficiency of 100% was achieved after 60 min of photocatalytic oxidation reaction UV 254 nm	[86]
Fe_2O_3-Fe_3O_4 nanoparticles (NIO) supported in montmorillonite (NIOM)	MO	PCPO	NIOM exhibited a higher photocatalytic activity compared with Fe_2O_3–Fe_3O_4	[202]
Fe_2O_3/kaolin	Rhodamine B (RhB)	PCPO	DE of 98% by using 1 g/L of catalyst and 0.05 mol/L of H_2O_2 for 120 min. The Fe_2O_3–kaolin catalyst displayed high photocatalytic activity in a wide pH range of 2.21–10.13	

7. Conclusions and Future Perspective

AOPs are promising methods and advanced treatment processes for the degradation and mineralization of various pollutants, either in air or in water; particularly, AOPs have attracted considerable interest for wastewater treatment. The most extensively studied AOPs are catalytic oxidation, catalytic wet peroxidation, photocatalysis, and photooxidation, which have demonstrated their efficiency in the removal of recalcitrant compounds from pollutants. The immobilization of semiconductors or metal/metal oxide nanoparticles on clay structures is one such effort to support and enhance the effectiveness of the catalytic process. Although the uses of clay-supported metal/metal oxide nanoparticles in AOPs are highly successful at laboratory scales, there are not many successful examples of their applicability at industrial scales. The economic viability and efficiency of AOPs are key factors that limit their industrial applications. Such pilot schemes for nanocomposite setups at larger scales require considerable optimization and face some adaptations from the laboratory scale. In addition, the synthesis of clay-based nanocomposite is usually evaluated in relation to the long synthesis process and its reproducibility in larger amounts. Minimizing water intensification for the synthesis is the aspect that requires the most consideration. However, compared with some other inorganic supports for metal/metal oxides, such as mesoporous silica, synthetic zeolite, alumina, carbon, and graphene, the use of clay minerals in this study summarizes the existing higher potential for the AOP treatments, from perspectives of cost and resource use. Future studies should focus on the intensification of scaling-up the applications of clay-supported metal/metal oxide to develop effective and low-cost AOPs. This will be useful to support small- and medium-scale industries that release pollutants.

References

1. Leal Filho, W.; Totin, E.; Franke, J.A.; Andrew, S.M.; Abubakar, I.R.; Azadi, H.; Nunn, P.D.; Ouweneel, B.; Williams, P.A.; Simpson, N.P. Understanding responses to climate-related water scarcity in Africa. *Sci. Total Environ.* **2022**, *806*, 150420. [CrossRef]

2. Antonelli, M.; Greco, F. *The Water We Eat: Combining Virtual Water and Water Footprints*; Springer International Publishing: Cham, Switzerland, 2015; pp. 1–256. [CrossRef]

3. Alcon, F.; Zabala, J.A.; Martínez-García, V.; Albaladejo, J.A.; López-Becerra, E.I.; de-Miguel, M.D.; Martínez-Paz, J.M. The social wellbeing of irrigation water. A demand-side integrated valuation in a Mediterranean agroecosystem. *Agric. Water Manag.* **2022**, *262*, 107400. [CrossRef]

4. Carmen, Z.; Daniel, S. Textile Organic Dyes—Characteristics, Polluting Effects and Separation/Elimination Procedures from Industrial Effluents—A Critical Overview. In *Organic Pollutants Ten Years After the Stockholm Convention—Environmental and Analytical Update*; IntechOpen: London, UK, 2012. [CrossRef]

5. Ince, N.H. Ultrasound-assisted advanced oxidation processes for water decontamination. *Ultrason. Sonochem.* **2018**, *40*, 97–103. [CrossRef] [PubMed]

6. Inayat, A.; Said, Z.; Alsaidi, O.; Al-Zaidi, R.; Ullah, S.; Stathopoulos, V. Review of Recent Progress in Wastewater Treatment Using Carbon Nanotubes. *Curr. Anal. Chem.* **2021**, *17*, 20–30. [CrossRef]

7. Bergamasco, R.; Konradt-Moraes, L.C.; Vieira, M.F.; Fagundes-Klen, M.R.; Vieira, A.M.S. Performance of a coagulation–ultrafiltration hybrid process for water supply treatment. *Chem. Eng. J.* **2011**, *166*, 483–489. [CrossRef]

8. Chen, Z.; Zheng, R.; Wei, W.; Wei, W.; Zou, W.; Li, J.; Ni, B.-J.; Chen, H. Recycling spent water treatment adsorbents for efficient electrocatalytic water oxidation reaction. *Resour. Conserv. Recycl.* **2022**, *178*, 106037. [CrossRef]

9. Camargo-Perea, A.L.; Rubio-Clemente, A.; Peñuela, G.A. Use of Ultrasound as an Advanced Oxidation Process for the Degradation of Emerging Pollutants in Water. *Water* **2020**, *12*, 1068. [CrossRef]

10. Zuorro, A.; Lavecchia, R.; Monaco, M.M.; Iervolino, G.; Vaiano, V. Photocatalytic degradation of azo dye reactive violet 5 on Fe-doped titania catalysts under visible light irradiation. *Catalysts* **2019**, *9*, 645. [CrossRef]

11. Zhang, Z.; Xu, Y.; Ma, X.; Li, F.; Liu, D.; Chen, Z.; Zhang, F.; Dionysiou, D.D. Microwave degradation of methyl orange dye in aqueous solution in the presence of nano-TiO_2-supported activated carbon (supported-TiO_2/AC/MW). *J. Hazard. Mater.* **2012**, *209–210*, 271–277. [CrossRef]

12. Zhang, L.; Liu, X.; Guo, X.; Su, M.; Xu, T.; Song, X. Investigation on the degradation of brilliant green induced oxidation by $NiFe_2O_4$ under microwave irradiation. *Chem. Eng. J.* **2011**, *173*, 737–742. [CrossRef]

13. Velempini, T.; Prabakaran, E.; Pillay, K. Recent developments in the use of metal oxides for photocatalytic degradation of pharmaceutical pollutants in water—A review. *Mater. Today Chem.* **2021**, *19*, 100380. [CrossRef]

14. Al-Hamdi, A.M.; Rinner, U.; Sillanpää, M. Tin dioxide as a photocatalyst for water treatment: A review. *Process Saf. Environ. Prot.* **2017**, *107*, 190–205. [CrossRef]

15. Naseem, T.; Durrani, T. The role of some important metal oxide nanoparticles for wastewater and antibacterial applications: A review. *Environ. Chem. Ecotoxicol.* **2021**, *3*, 59–75. [CrossRef]

16. Sarkar, S.; Guibal, E.; Quignard, F.; SenGupta, A.K. Polymer-supported metals and metal oxide nanoparticles: Synthesis, characterization, and applications. *J. Nanoparticle Res.* **2012**, *14*, 715. [CrossRef]

17. Biswas, S.; Pal, A.; Pal, T. Supported metal and metal oxide particles with proximity effect for catalysis. *RSC Adv.* **2020**, *10*, 35449–35472. [CrossRef]

18. Khraisheh, M.; Elhenawy, S.; Almomani, F.; Al-ghouti, M. Recent Progress on Nanomaterial-Based Membranes for Water Treatment. *Membranes* **2021**, *11*, 995. [CrossRef]

19. da Cunha, T.; Maulu, A.; Guillot, J.; Fleming, Y.; Duez, B.; Lenoble, D.; Arl, D. Design of silica nanoparticles-supported metal catalyst by wet impregnation with catalytic performance for tuning carbon nanotubes growth. *Catalysts* **2021**, *11*, 986. [CrossRef]

20. Hou, Y.X.; Abdullah, H.; Kuo, D.H.; Leu, S.J.; Gultom, N.S.; Su, C.H. A comparison study of SiO_2/nano metal oxide composite sphere for antibacterial application. *Compos. Part B Eng.* **2018**, *133*, 166–176. [CrossRef]

21.　Kumar, J.P.; Ramacharyulu, P.V.R.K.; Prasad, G.K.; Singh, B. Montmorillonites supported with metal oxide nanoparticles for decontamination of sulfur mustard. *Appl. Clay Sci.* **2015**, *116–117*, 263–272. [CrossRef]

22.　Manos, G.; Yusof, I.Y.; Papayannakos, N.; Gangas, N.H. Catalytic Cracking of Polyethylene over Clay Catalysts. Comparison with an Ultrastable Y Zeolite. *Ind. Eng. Chem. Res.* **2001**, *40*, 2220–2225. [CrossRef]

23.　Kumar, B.S.; Dhakshinamoorthy, A.; Pitchumani, K. K10 montmorillonite clays as environmentally benign catalysts for organic reactions. *Catal. Sci. Technol.* **2014**, *4*, 2378–2396. [CrossRef]

24.　Xu, A.; Yang, M.; Yao, H.; Du, H.; Sun, C. Rectorite as catalyst for wet air oxidation of phenol. *Appl. Clay Sci.* **2009**, *43*, 435–438. [CrossRef]

25.　Prakash, B.J.; Bhat, Y.S.; Reddy, C.R. Clays as sustainable catalysts for organic transformations. *Clay Types Prop. Uses* **2011**, *63*, 44.

26.　Cuerda-Correa, E.M.; Alexandre-Franco, M.F.; Fernández-González, C. Advanced oxidation processes for the removal of antibiotics from water. An overview. *Water* **2020**, *12*, 102. [CrossRef]

27.　Xia, X.; Zhu, F.; Li, J.; Yang, H.; Wei, L.; Li, Q.; Jiang, J.; Zhang, G.; Zhao, Q. A Review Study on Sulfate-Radical-Based Advanced Oxidation Processes for Domestic/Industrial Wastewater Treatment: Degradation, Efficiency, and Mechanism. *Front. Chem.* **2020**, *8*, 1092. [CrossRef]

28.　Lian, L.; Yao, B.; Hou, S.; Fang, J.; Yan, S.; Song, W. Kinetic Study of Hydroxyl and Sulfate Radical-Mediated Oxidation of Pharmaceuticals in Wastewater Effluents. *Environ. Sci. Technol.* **2017**, *51*, 2954–2962. [CrossRef]

29.　Nihemaiti, M.; Permala, R.R.; Reactivity, J.C. Reactivity of Unactivated Peroxymonosulfate with Nitrogenous Compounds. *Water Res.* **2020**, *169*, 115221. [CrossRef]

30.　Xiao, G.; Xu, T.; Faheem, M.; Xi, Y.; Zhou, T.; Moryani, H.T.; Bao, J.; Du, J. Evolution of singlet oxygen by activating peroxydisulfate and peroxymonosulfate: A review. *Int. J. Environ. Res. Public Health* **2021**, *18*, 3344. [CrossRef]

31.　Processes, O. Oxidation Processes. In *Metal-Oxygen Clusters. Fundamental and Applied Catalysis*; Springer: Boston, MA, USA, 2002; pp. 227–288. [CrossRef]

32.　Argyle, M.D.; Bartholomew, C.H. Heterogeneous catalyst deactivation and regeneration: A review. *Catalysts* **2015**, *5*, 145–269. [CrossRef]

33.　Stampfl, C.; Veronica Ganduglia-Pirovano, M.; Reuter, K.; Scheffler, M. Catalysis and corrosion: The theoretical surface-science context. *Surf. Sci.* **2002**, *500*, 368–394. [CrossRef]

34.　Deng, Y.; Zhao, R. Advanced Oxidation Processes (AOPs) in Wastewater Treatment. *Curr. Pollut. Rep.* **2015**, *1*, 167–176. [CrossRef]

35.　Giwa, A.; Yusuf, A.; Balogun, H.A.; Sambudi, N.S.; Bilad, M.R.; Adeyemi, I.; Chakraborty, S.; Curcio, S. Recent advances in advanced oxidation processes for removal of contaminants from water: A comprehensive review. *Process Saf. Environ. Prot.* **2021**, *146*, 220–256. [CrossRef]

36.　Orlov, A.; Klinowski, J. Oxidation of volatile organic compounds on SBA-15 mesoporous molecular sieves modified with manganese. *Chemosphere* **2009**, *74*, 344–348. [CrossRef] [PubMed]

37.　Liu, Y.; Shen, J.; Zhao, L.; Wang, W.; Gong, W.; Zheng, F. Zinc-iron silicate for heterogeneous catalytic ozonation of acrylic acid: Efficiency and mechanism. *RSC Adv.* **2020**, *10*, 9146–9154. [CrossRef]

38.　Pirilä, M.; Saouabe, M.; Ojala, S.; Rathnayake, B.; Drault, F.; Valtanen, A.; Huuhtanen, M.; Brahmi, R.; Keiski, R.L. Photocatalytic degradation of organic pollutants in wastewater. *Top. Catal.* **2015**, *58*, 1085–1099. [CrossRef]

39.　Sagadevan, S.; Imteyaz, S.; Murugan, B.; Lett, J.A.; Sridevi, N.; Weldegebrieal, G.K.; Fatimah, I.; Oh, W.-C. A comprehensive review of green synthesis of titanium dioxide nanoparticles and their diverse biomedical applications. *Inorg. Chem. Commun.* **2022**, *11*, 44–63. [CrossRef]

40.　Rokesh, K.; Mohan, S.C.; Karuppuchamy, S.; Jothivenkatachalam, K. Photo-assisted advanced oxidation processes for Rhodamine B degradation using ZnO-Ag nanocomposite materials. *J. Environ. Chem. Eng.* **2016**, *6*, 3610–3620. [CrossRef]

41.　Karthik, R.; Govindasamy, M.; Chen, S.M.; Cheng, Y.H.; Muthukrishnan, P.; Padmavathy, S.; Elangovan, A. Biosynthesis of silver nanoparticles by using Camellia japonica leaf extract for the electrocatalytic reduction of nitrobenzene and photocatalytic degradation of Eosin-Y. *J. Photochem. Photobiol. B Biol.* **2017**, *170*, 164–172. [CrossRef]

42.　Wang, H.; Peng, D.; Chen, T.; Chang, Y.; Dong, S. A novel photocatalyst AgBr/ZnO/RGO with high visible light photocatalytic activity. *Ceram. Int.* **2016**, *42*, 4406–4412. [CrossRef]

43.　Dong, P.; Hou, G.; Liu, C.; Zhang, X.; Tian, H.; Xu, F.; Xi, X.; Shao, R. Origin of activity and stability enhancement for Ag_3PO_4 photocatalyst after calcination. *Materials* **2016**, *9*, 968. [CrossRef]

44.　Akbari, A.; Sabouri, Z.; Hosseini, H.A.; Hashemzadeh, A.; Khatami, M.; Darroudi, M. Effect of nickel oxide nanoparticles as a photocatalyst in dyes degradation and evaluation of effective parameters in their removal from aqueous environments. *Inorg. Chem. Commun.* **2020**, *115*, 107867. [CrossRef]

45.　Angel Ezhilarasi, A.; Judith Vijaya, J.; Kaviyarasu, K.; John Kennedy, L.; Ramalingam, R.J.; Al-Lohedan, H.A. Green synthesis of NiO nanoparticles using Aegle marmelos leaf extract for the evaluation of in-vitro cytotoxicity, antibacterial and photocatalytic properties. *J. Photochem. Photobiol. B Biol.* **2018**, *180*, 39–50. [CrossRef] [PubMed]

46.　Ketteler, G.; Weiss, W.; Ranke, W.; Schlögl, R. Bulk and surface phases of iron oxides in oxygen and water atmosphere at low pressure. *R. Phys. Chem. Chem. Phys.* **2001**, *3*, 1114–1122. [CrossRef]

47.　Karim, W.; Kleibert, A.; Hartfelder, U.; Balan, A.; Gobrecht, H.; Bokhoven, J.A.; Ekinci, Y. Size-dependent redox behavior of iron observed by in-situ single nanoparticle spectro-microscopy on well-defined model systems. *Sci. Rep.* **2016**, *6*, 18818. [CrossRef] [PubMed]

48. Debnath, B.; Roy, A.S.; Kapri, S.; Bhattacharyya, S. Efficient Dye Degradation Catalyzed by Manganese Oxide Nanoparticles and the Role of Cation Valence. *ChemistrySelect* **2016**, *1*, 4265–4273. [CrossRef]

49. Bagheri, M.; Najafabadi, N.R.; Borna, E. Removal of reactive blue 203 dye photocatalytic using ZnO nanoparticles stabilized on functionalized MWCNTs. *J. King Saud Univ.—Sci.* **2020**, *32*, 799–804. [CrossRef]

50. Yao, Y.R.; Zheng, Y.; Song, X.C. Catalytic degradation of phenol by γ-Fe_2O_3 nanoparticles. *Adv. Mater. Res.* **2014**, *887–888*, 139–142. [CrossRef]

51. Kusior, A.; Michalec, K.; Jelen, P.; Radecka, M. Shaped Fe_2O_3 nanoparticles—Synthesis and enhanced photocatalytic degradation towards RhB. *Appl. Surf. Sci.* **2019**, *476*, 342–352. [CrossRef]

52. Nayak, R.; Ali, F.A.; Mishra, D.K.; Ray, D.; Aswal, V.K.; Sahoo, S.K.; Nanda, B. Fabrication of CuO nanoparticle: An efficient catalyst utilized for sensing and degradation of phenol. *J. Mater. Res. Technol.* **2020**, *9*, 11045–11059. [CrossRef]

53. Najjar, M.; Hosseini, H.A.; Masoudi, A.; Hashemzadeh, A.; Darroudi, M. Preparation of tin oxide (IV) nanoparticles by a green chemistry method and investigation of its role in the removal of organic dyes in water purification. *Res. Chem. Intermed.* **2020**, *46*, 2155–2168. [CrossRef]

54. Abdullah, H.; Ariyanto, N.P.; Shaari, S.; Yuliarto, B.; Junaidi, S. Study of Porous Nanoflake ZnO for Dye-Sensitized Solar Cell Application. *Am. J. Eng. Appl. Sci.* **2009**, *2*, 236–240. [CrossRef]

55. Mudusu, D.; Nandanapalli, K.R.; Dugasani, S.R.; Park, S.H.; Tu, C.W. Zinc oxide nanorods shielded with an Ultrathin Nickel layer: Tailoring of physical properties. *Sci. Rep.* **2016**, *6*, 28561. [CrossRef] [PubMed]

56. Ghannam, H.; Chahboun, A.; Turmine, M. Wettability of zinc oxide nanorod surfaces. *RSC Adv.* **2019**, *9*, 38289–38297. [CrossRef]

57. Sofianos, V.M.; Lee, J.; Silvester, D.D.; .Samanta, P.K.; Paskevicius, M.; English, N.J.; Buckley, C.E. Diverse morphologies of zinc oxide nanoparticles and their electrocatalytic performance in hydrogen production. *J. Energ. Chem.* **2021**, *56*, 162–170. [CrossRef]

58. Ridhuan, N.S.; Abdul Razak, K.; Lockman, Z.; Abdul Aziz, A. Structural and Morphology of ZnO Nanorods Synthesized Using ZnO Seeded Growth Hydrothermal Method and Its Properties as UV Sensing. *PLoS ONE* **2012**, *7*, e50405. [CrossRef]

59. Perumal, V.; Hashim, U.; Gopinath, S.C.; Haarindraprasad, R.; Foo, K.L.; Balakrishnan, S.R.; Poopalan, P. 'Spotted Nanoflowers': Gold-seeded Zinc Oxide Nanohybrid for Selective Bio-capture. *Sci. Rep.* **2015**, *5*, 12231. [CrossRef]

60. Lin, J.H.; Patil, R.A.; Devan, R.S.; Liu, Z.A.; Wang, Y.P.; Ho, C.H.; Liou, Y.; Ma, Y.R. Photoluminescence mechanisms of metallic Zn nanospheres, semiconducting ZnO nanoballoons and metal-semiconductor Zn/ZnO nanospheres. *Sci. Rep.* **2014**, *4*, 6967. [CrossRef]

61. Kołodziejczak-Radzimska, A.; Jesionowski, T. Zinc Oxide—From Synthesis to Application: A Review. *Materials* **2014**, *7*, 2833–2881. [CrossRef]

62. Bundschuh, M.; Filser, J.; Lüderwald, S.; McKee, M.S.; Metreveli, G.; Schaumann, G.E.; Schulz, R.; Wagner, S. Nanoparticles in the environment: Where do we come from, where do we go to? *Environ. Sci. Eur.* **2018**, *30*, 6. [CrossRef]

63. Taghavi, S.M.; Momenpour, M.; Azarian, M.; Ahmadian, M.; Souri, F.; Taghavi, S.A.; Sadeghain, M.; Karchani, M. Effects of Nanoparticles on the Environment and Outdoor Workplaces. *Electron. Physician* **2013**, *5*, 706–712. [CrossRef]

64. Asif, S.A.B.; Khan, S.B.; Asiri, A.M. Efficient solar photocatalyst based on cobalt oxide/iron oxide composite nanofibers for the detoxification of organic pollutants. *Nanoscale Res. Lett.* **2014**, *9*, 510. [CrossRef] [PubMed]

65. Wei, W.D.; Liu, X.Y.; Cui, S.C.; Liu, J.G. Loading of Co_3O_4 onto Pt-modified nitrogen-doped TiO_2 nanocomposites promotes photocatalytic hydrogen production. *RSC Adv.* **2017**, *7*, 25650–25656. [CrossRef]

66. Iazdani, F.; Nezamzadeh-Ejhieh, A. The photocatalytic rate of ZnO supported onto natural zeolite nanoparticles in the photodegradation of an aromatic amine. *Environ. Sci. Pollut. Res.* **2021**, *28*, 53314–53327. [CrossRef] [PubMed]

67. Gayatri, R.; Agustina, T.E.; Bahrin, D.; Moeksin, R.; Gustini, G. Preparation and Characterization of ZnO-Zeolite Nanocomposite for Photocatalytic Degradation by Ultraviolet Light. *J. Ecol. Eng.* **2020**, *22*, 178–186. [CrossRef]

68. Jahangirian, H.; Rafiee-Moghaddam, R.; Jahangirian, N.; Nikpey, B.; Jahangirian, S.; Bassous, N.; Saleh, B.; Kalantari, K.; Webster, T.J. Green synthesis of zeolite/Fe_2O_3 nanocomposites: Toxicity & cell proliferation assays and application as a smart iron nanofertilizer. *Int. J. Nanomed.* **2020**, *15*, 1005–1020. [CrossRef]

69. Taghvaei, H.; Farhadian, M.; Davari, N.; Maazi, S. Preparation, characterization and photocatalytic degradation of methylene blue by Fe^{3+} doped TiO_2 supported on natural zeolite using response surface methodology. *Adv. Environ. Technol.* **2017**, *3*, 205–216. [CrossRef]

70. Su, R.; Tiruvalam, R.; Logsdail, A.J.; He, Q.; Downing, C.A.; Jensen, M.T.; Dimitratos, N.; Kesavan, L.; Wells, P.P.; Bechstein, R.; et al. Designer Titania-Supported Au À Pd Nanoparticles for Efficient Photocatalytic Hydrogen Production. *ACS Nano* **2014**, *8*, 3490–3497. [CrossRef]

71. Hirakawa, H.; Shiota, S.; Shiraishi, Y.; Sakamoto, H.; Ichikawa, S.; Hirai, T. Au Nanoparticles Supported on $BiVO_4$: Effective Inorganic Photocatalysts for H_2O_2 Production from Water and O_2 under Visible Light. *ACS Catal.* **2016**, *6*, 4976–4982. [CrossRef]

72. Radhika, N.P.; Selvin, R.; Kakkar, R.; Umar, A. Recent advances in nano-photocatalysts for organic synthesis. *Arab. J. Chem.* **2019**, *12*, 4550–4578. [CrossRef]

73. Madni, A.; Noreen, S.; Maqbool, I.; Rehman, F.; Batool, A.; Kashif, P.M.; Rehman, M.; Tahir, N.; Khan, M.I. Graphene-based nanocomposites: Synthesis and their theranostic applications. *J. Drug Target.* **2018**, *26*, 858–883. [CrossRef]

74. Li, X.; Yu, J.; Wageh, S.; Al-Ghamdi, A.A.; Xie, J. Graphene in Photocatalysis: A Review. *Small* **2016**, *12*, 6640–6696. [CrossRef] [PubMed]

75. Song, B.T.; Long, N.V.; Hang, N.T.N. The development of biomass-derived carbon based photocatalysts for visible-light-driven photodegradation of pollutants: A comprehensive review. *RSC Adv.* **2021**, *11*, 30574.

76. Li, L.; Yu, Y.; Lin, S.; Chu, W.; Sun, D.; Su, Q.; Ma, S.; Du, G.; Xu, B. Single ruthenium atom supported on g-C$_3$N$_4$ as an efficient photocatalyst for nitrogen fixation in ultra-pure water. *Catal. Commun.* **2021**, *153*, 106294. [CrossRef]

77. Quintanilla, A.; García-Rodríguez, S.; Domínguez, C.M.; Blasco, S.; Casas, J.A.; Rodriguez, J.J. Supported gold nanoparticle catalysts for wet peroxide oxidation. *Appl. Catal. B Environ.* **2012**, *111–112*, 81–89. [CrossRef]

78. Wang, J.; Farias, J.; Tiwary, A.; Tangyie, G.C.; Huddersman, K. Advance Oxidation Process (AOP) of Bisphenol A Using a Novel Surface-Functionalised Polyacrylonitrile (PAN) Fibre Catalyst. *Water* **2022**, *14*, 640. [CrossRef]

79. Zhang, G.; Gao, Y.; Zhang, Y.; Guo, Y. Fe$_2$O$_3$-pillared rectorite as an efficient and stable fenton-like heterogeneous catalyst for photodegradation of organic contaminants. *Environ. Sci. Technol.* **2010**, *44*, 6384–6389. [CrossRef]

80. Kokkinos, P.; Venieri, D.; Mantzavinos, D. Advanced Oxidation Processes for Water and Wastewater Viral Disinfection. A Systematic Review. *Food Environ. Virol. 2021. 13*, 283–302. [CrossRef]

81. Misra, A.J.; Das, S.; Habeeb Rahman, A.P.; Das, B.; Jayabalan, R.; Behera, S.K.; Suar, M.; Tamhankar, A.J.; Mishra, A.; Lundborg, C.S.; et al. Doped ZnO nanoparticles impregnated on Kaolinite (Clay): A reusable nanocomposite for photocatalytic disinfection of multidrug resistant *Enterobacter* sp. under visible light. *J. Colloid Interface Sci.* **2018**, *530*, 610–623. [CrossRef]

82. Mukherjee, S. Classification and Composition of Clay Constituents. In *The Science of Clays*; Springer: Dordrecht, The Netherlands, 2013; pp. 23–32. [CrossRef]

83. Cecilia, J.A.; García-Sancho, C.; Vilarrasa-García, E.; Jiménez-Jiménez, J.; Rodriguez-Castellón, E. Synthesis, Characterization, Uses and Applications of Porous Clays Heterostructures: A Review. *Chem. Rec.* **2018**, *18*, 1085–1104. [CrossRef]

84. Zhou, C.H. An overview on strategies towards clay-based designer catalysts for green and sustainable catalysis. *Appl. Clay Sci.* **2011**, *53*, 87–96. [CrossRef]

85. Serwicka, E.M. Titania-clay mineral composites for environmental catalysis and photocatalysis. *Catalysts* **2021**, *11*, 1087. [CrossRef]

86. Hadjltaief, H.B.; Da Costa, P.; Beaunier, P.; Gálvez, M.E.; Zina, M.B. Fe-clay-plate as a heterogeneous catalyst in photo-Fenton oxidation of phenol as probe molecule for water treatment. *Appl. Clay Sci.* **2014**, *91–92*, 46–54. [CrossRef]

87. Bhattacharyya, K.G.; Gupta, S. Sen Kaolinite, montmorillonite, and their modified derivatives as adsorbents for removal of Cu(II) from aqueous solution. *Sep. Purif. Technol.* **2006**, *50*, 388–397. [CrossRef]

88. Detellier, C. Functional Kaolinite. *Chem. Rec.* **2018**, *18*, 868–877. [CrossRef]

89. Dedzo, G.K.; Detellier, C. Functional nanohybrid materials derived from kaolinite. *Appl. Clay Sci.* **2016**, *130*, 33–39. [CrossRef]

90. Hettinger, W.P. Contribution to catalytic cracking in the petroleum industry. *Appl. Clay Sci.* **1991**, *5*, 445–468. [CrossRef]

91. Bahulayan, D.; John, L.; Lalithambika, M. Modified clays as efficient acid-base catalyst systems for diazotization and diazocoupling reactions. *Synth. Commun.* **2003**, *33*, 863–869. [CrossRef]

92. Liu, J.; Yun, Z.; Gui, X. CE/Kaolin clay as an active catalyst for fatty acid methyl esters production from cottonseed oil in a new integrated apparatus. *Braz. J. Chem. Eng.* **2018**, *35*, 147–154. [CrossRef]

93. Alves, H.J.; da Rocha, A.M.; Monteiro, M.R.; Moretti, C.; Cabrelon, M.D.; Schwengber, C.A.; Milinsk, M.C. Treatment of clay with KF: New solid catalyst for biodiesel production. *Appl. Clay Sci.* **2014**, *91–92*, 98–104. [CrossRef]

94. Parida, K.; Varadwaj, G.B.B.; Sahu, S.; Sahoo, P.C. Schiff base Pt(II) complex intercalated montmorillonite: A robust catalyst for hydrogenation of aromatic nitro compounds at room temperature. *Ind. Eng. Chem. Res.* **2011**, *50*, 7849–7856. [CrossRef]

95. Nagendrappa, G. Organic synthesis using clay and clay-supported catalysts. *Appl. Clay Sci.* **2011**, *53*, 106–138. [CrossRef]

96. Fatimah, I.; Rubiyanto, D.; Prakoso, N.I.; Yahya, A.; Sim, Y.-L. Green conversion of citral and citronellal using tris(bipyridine)ruthenium(II)-supported saponite catalyst under microwave irradiation. *Sustain. Chem. Pharm.* **2019**, *11*, 61–70. [CrossRef]

97. Mora, L.D.; Bonfim, L.F.; Barbosa, L.V.; da SIlva, T.H.; Nassar, E.J.; Ciuffi, K.J.; Gonzalez, B.; Vincente, M.A.; Trujillano, R.; Rives, V.; et al. White and Red Braxilian Sao Siamao's Kaolinite-TiO$_2$ Nanocomposites as Catalysts for Toluene Photodegradation from Aqueous Solutions. *Materials* **2019**, *12*, 3943. [CrossRef] [PubMed]

98. Kočí, K.; Matějka, V.; Kovář, P.; Lacný, Z.; Obalová, L. Comparison of the pure TiO$_2$ and kaolinite/TiO$_2$ composite as catalyst for CO$_2$ photocatalytic reduction. *Catal. Today* **2011**, *161*, 105–109. [CrossRef]

99. He, Y.; Jiang, D.; Chen, J.; Jiang, D.Y.; Zhang, Y.X. Synthesis of MnO$_2$ nanosheets on montmorillonite for oxidative degradation and adsorption of methylene blue. *J. Colloid Interface Sci.* **2018**, *510*, 207–220. [CrossRef]

100. He, Q.; Xie, C.; Gan, D.; Xiao, C. The efficient degradation of organic pollutants in an aqueous environment under visible light irradiation by persulfate catalytically activated with kaolin-Fe$_2$O$_3$. *RSC Adv.* **2019**, *10*, 43–52. [CrossRef]

101. Luna, F.M.T.; Cecilia, J.A.; Saboya, R.M.A.; Barrera, D.; Sapag, K.; Rodríguez-Castellón, E.; Cavalcante, C.L. Natural and modified montmorillonite clays as catalysts for synthesis of biolubricants. *Materials* **2018**, *11*, 1764. [CrossRef]

102. Vidal, C.B.; dos Santos, A.B.; do Nascimento, R.F.; Bandosz, T.J. Reactive adsorption of pharmaceuticals on tin oxide pillared montmorillonite: Effect of visible light exposure. *Chem. Eng. J.* **2015**, *259*, 865–875. [CrossRef]

103. Sadykov, V.A.; Kuznetsova, T.G.; Doronin, V.P.; Sorokina, T.P.; Alikina, G.M.; Kochubei, D.I.; Novgorodov, B.N.; Paukshtis, E.A.; Fenelonov, V.B.; Zaikovskii, V.I.; et al. Zirconia Pillared Clays: Synthesis, Characterization and Catalytic Properties in the NOx Selective Reduction by Hydrocarbons in the Oxygen Excess. *Chem. Sustain. Dev.* **2003**, *11*, 249–262.

104. Chaabene, S.B.; Bergaoui, L.; Ghorbel, A. Zirconium and sulfated zirconium pillared clays: A combined intercalation solution study and solid characterization. *Colloids Surf. A Physicochem. Eng. Asp.* **2004**, *251*, 109–115. [CrossRef]

105. Cardona, Y.; Vicente, M.A.; Korili, S.A.; Gil, A. Progress and perspectives for the use of pillared clays as adsorbents for organic compounds in aqueous solution. *Rev. Chem. Eng.* **2020**. [CrossRef]

106. Tireli, A.A.; Marcos, F.C.F.; Oliveira, L.F.; do Guimarães, I.R.; Guerreiro, M.C.; Silva, J.P. Influence of magnetic field on the adsorption of organic compound by clays modified with iron. *Appl. Clay Sci.* **2014**, *97–98*, 1–7. [CrossRef]

107. Chen, Q.; Wu, P.; Li, Y.; Zhu, N.; Dang, Z. Heterogeneous photo-Fenton photodegradation of reactive brilliant orange X-GN over iron-pillared montmorillonite under visible irradiation. *J. Hazard. Mater.* **2009**, *168*, 901–908. [CrossRef]

108. Kloprogge, J.T.; Evans, R.; Hickey, L.; Frost, L. Characterisation and Al-pillaring of smectites from Miles, Queensland (Australia). *Appl. Clay Sci.* **2002**, *20*, 157–163. [CrossRef]

109. Kloprogge, J.T.; Duong, L.V.; Frost, R.L. A review of the synthesis and characterisation of pillared clays and related porous materials for cracking of vegetable oils to produce biofuels. *Environ. Geol.* **2005**, *47*, 967–981. [CrossRef]

110. Undabeytia, T.; Galán-Jiménez, M.C.; Gómez-Pantoja, E.; Vázquez, J.; Casal, B.; Bergaya, F.; Morillo, E. Fe-pillared clay mineral-based formulations of imazaquin for reduced leaching in soil. *Appl. Clay Sci.* **2013**, *80–81*, 382–389. [CrossRef]

111. De León, M.A.; Rodríguez, M.; Marchetti, S.G.; Sapag, K.; Faccio, R.; Sergio, M.; Bussi, J. Raw montmorillonite modified with iron for photo-Fenton processes: Influence of iron content on textural, structural and catalytic properties. *J. Environ. Chem. Eng.* **2017**, *5*, 4742–4750. [CrossRef]

112. Rigoti, E.; Schwanke, A.J.; Araújo, K.C.; Martínez-Huitle, C.A.; Pergher, S.B.C. Titanium oxide supported montmorillonite clays for environmental applications. *J. Mex. Chem. Soc.* **2019**, *63*, 1–12. [CrossRef]

113. Lu, P.; Liang, C.; Wei, Y.; Song, Z. New design for titanium-pillared montmorillonite composites as efficient heterogeneous catalysts to enhance Fe(II) reductivity for 2-nitrophenol removal. *Appl. Clay Sci.* **2021**, *205*, 106052. [CrossRef]

114. Vercellone, S.Z.; Sham, E.; Torres, E.M.F. Measure of Zeta Potential of Titanium Pillared Clays. *Procedia Mater. Sci.* **2015**, *8*, 599–607. [CrossRef]

115. Vicente, M.A.; Bañares-Muñoz, M.A.; Toranzo, R.; Gandía, L.M.; Gil, A. Influence of the Ti precursor on the properties of Ti–pillared smectites. *Clay Miner.* **2001**, *36*, 125–138. [CrossRef]

116. Al-Beladi, A.A.; Kosa, S.A.; Wahab, R.A.; Salam, M.A. Removal of orange G dye from water using halloysite nanoclay-supported ZnO nanoparticles. *Desalin. Water Treat.* **2020**, *196*, 287–298. [CrossRef]

117. Xu, H.; Zhang, D.; Xu, A.; Wu, F.; Cao, R. Quantum Sized Zinc Oxide Immobilized on Bentonite Clay and Degradation of C.I. Acid Red 35 in Aqueous under Ultraviolet Light. *Int. J. Photoenergy* **2015**, *2015*, 750869. [CrossRef]

118. Butman, M.F.; Ovchinnikov, N.L.; Karasev, N.S.; Kochkina, N.E.; Agafonov, A.V.; Vinogradov, A.V. Photocatalytic and adsorption properties of TiO_2-pillared montmorillonite obtained by hydrothermally activated intercalation of titanium polyhydroxo complexes. *Beilstein J. Nanotechnol.* **2018**, *9*, 364–379. [CrossRef] [PubMed]

119. Ravari, M.H.; Sarrafi, A.; Tahmooresi, M. Synthesizing and characterizing the mixed Al,Cu-pillared and copper doped Al-pillared bentonite for electrocatalytic reduction of CO_2. *S. Afr. J. Chem. Eng.* **2020**, *31*, 1–6. [CrossRef]

120. Guimarães, V.; Teixeira, A.R.; Lucas, M.S.; Peres, J.A. Effect of Zr Impregnation on Clay-Based Materials for H_2O_2-Assisted Photocatalytic Wet Oxidation of Winery Wastewater. *Water* **2020**, *12*, 3387. [CrossRef]

121. Timofeeva, M.N.; Malyshev, M.E.; Panchenko, V.N.; Shmakov, A.N.; Potapov, A.G.; Mel'gunov, M.S. $FeAl_{12}$-Keggin type cation as an active site source for Fe,Al-silica mesoporous catalysts. *Appl. Catal. B Environ.* **2010**, *95*, 110–119. [CrossRef]

122. Romero, A.; Dorado, F.; Asencio, I.; García, P.B.; Valverde, J.L. Ti-pillared clays: Synthesis and general characterization. *Clays Clay Miner.* **2006**, *54*, 737–747. [CrossRef]

123. Fatimah, I.; Nurkholifah, Y.Y. Physicochemical and photocatalytic properties of Fe-pillared bentonite at various fe content. *Bull. Chem. React. Eng. Catal.* **2016**, *11*, 398–405. [CrossRef]

124. Valverde, J.L.; Romero, A.; Romero, R.; García, P.B.; Sánchez, M.L.; Asencio, I. Preparation and characterization of Fe-PILCS. Influence of the synthesis parameters. *Clays Clay Miner.* **2005**, *53*, 613–621. [CrossRef]

125. Fatimah, I.; Rubiyanto, D.; Sahroni, I.; Putra, R.S.; Nurillahi, R.; Nugraha, J. Physicochemical characteristics and photocatalytic performance of Tin oxide/montmorillonite nanocomposites at various Sn/montmorillonite molar to mass ratios. *Appl. Clay Sci.* **2020**, *193*, 105671. [CrossRef]

126. Damardji, B.; Khalaf, H.; Duclaux, L.; David, B. Preparation of TiO_2-pillared montmorillonite as photocatalyst Part I. Microwave calcination, characterisation, and adsorption of a textile azo dye. *Appl. Clay Sci.* **2009**, *44*, 201–205. [CrossRef]

127. Munoz, H.-J.; Blanco, C.; Gil, A.; Vicente, M.-A.; Galeano, L.-A. Preparation of Al/Fe-Pillared Clays: Effect of the Starting Mineral. *Materials* **2017**, *10*, 1364. [CrossRef] [PubMed]

128. Galeano, L.A.; Gil, A.; Vicente, M.A. Effect of the atomic active metal ratio in Al/Fe-, Al/Cu- and Al/(Fe-Cu)-intercalating solutions on the physicochemical properties and catalytic activity of pillared clays in the CWPO of methyl orange. *Appl. Catal. B Environ.* **2010**, *100*, 271–281. [CrossRef]

129. Labib, I.; Boutoumi, H.; Khalaf, H. Synergistic effect of microwave calcination and sonophotocatalytic activity of TiO_2-montmorillonite on the degradation of direct yellow 106 and disperse violet 1. *Bull. Chem. React. Eng. Catal.* **2020**, *15*, 304–318. [CrossRef]

130. Minz, S.; Garg, S.; Gupta, R. Catalytic Wet Peroxide Oxidation of 4-Nitrophenol Over Al–Fe, Al–Cu and Al–Cu–Fe Pillared Clays. *Indian Chem. Eng.* **2018**, *60*, 16–36. [CrossRef]

131. Akkari, M.; Aranda, P.; Belver, C.; Bedia, J.; Ben Haj Amara, A.; Ruiz-Hitzky, E. ZnO/sepiolite heterostructured materials for solar photocatalytic degradation of pharmaceuticals in wastewater. *Appl. Clay Sci.* **2018**, *156*, 104–109. [CrossRef]

132. Babu, A.T.; Antony, R. Clay semiconductor hetero-system of SnO$_2$/bentonite nanocomposites for catalytic degradation of toxic organic wastes. *Appl. Clay Sci.* **2019**, *183*, 105312. [CrossRef]
133. Liu, R.; Ji, Z.; Wang, J.; Zhang, J. Mesocrystalline TiO$_2$/sepiolite composites for the effective degradation of methyl orange and methylene blue. *Front. Mater. Sci.* **2018**, *12*, 292–303. [CrossRef]
134. Ooka, C.; Yoshida, H.; Suzuki, K.; Hattori, T. Highly hydrophobic TiO$_2$ pillared clay for photocatalytic degradation of organic compounds in water. *Microporous Mesoporous Mater.* **2004**, *67*, 143–150. [CrossRef]
135. Khalfaoui-Boutoumi, N.; Boutoumi, N.; Khalaf, H.; David, B. Synthesis and characterization of TiO$_2$—Montmorillonite/Polythiophene-SDS nanocomposites: Application in the sonophotocatalytic degradation of rhodamine 6G. *Appl. Clay. Sci.* **2013**, *80–81*, 56–62. [CrossRef]
136. Ghnimi, S.M.; Srasra, N.F. Effect of Temperature Synthesis on the Catalytic Performance of Zirconium Pillared Interlayered Clays for Phenol Oxidation. *Mod. Chem. Appl.* **2017**, *5*, 1–9. [CrossRef]
137. Chen, D.; Zhu, Q.; Zhou, F.; Deng, X.; Li, F. Synthesis and photocatalytic performances of the TiO$_2$ pillared montmorillonite. *J. Hazard. Mater.* **2012**, *235–236*, 186–193. [CrossRef]
138. Ruiz-Hitzky, E.; Aranda, P.; Akkari, M.; Khaorapapong, N.; Ogawa, M. Photoactive nanoarchitectures based on clays incorporating TiO$_2$ and ZnO nanoparticles. *Beilstein J. Nanotechnol.* **2019**, *10*, 1140–1156. [CrossRef]
139. Sasikala, S.P.; Nibila, T.A.; Babitha, K.B.; Mohamed, A.A.P.; Solaiappan, A. Competitive photo-degradation performance of ZnO modified bentonite clay in water containing both organic and inorganic contaminants. *Sustain. Environ. Res.* **2019**, *29*, 1. [CrossRef]
140. Ruslan; Khairuddin; Hardi, J.; Mirzan, M. Characterization of zirconia-pillared clay with sulfate acid activation. In *AIP Conference Proceedings*; AIP Publishing LLC: Melville, NY, USA, 2020; Volume 2243. [CrossRef]
141. Sharma, S.; Sarasan, D.G. Influence of Acid Activation on Natural Calcium Montmorillonite Clay. *IOSR J. Appl. Chem.* **2017**, *10*, 71–77. [CrossRef]
142. Fatimah, I.; Purwiandono, G.; Citradewi, P.W.; Sagadevan, S.; Oh, W.C.; Doong, R.A. Influencing Factors in the Synthesis of Photoactive Nanocomposites of ZnO/SiO2-Porous Heterostructures from Montmorillonite and the Study for Methyl Violet Photodegradation. *Nanomaterials* **2021**, *11*, 3427. [CrossRef]
143. Kooli, F.; Hian, P.C.; Weirong, Q.; Alshahateet, S.F.; Chen, F. Effect of the acid-activated clays on the properties of porous clay heterostructures. *J. Porous Mater.* **2006**, *13*, 319–324. [CrossRef]
144. Taher, T.; Mohadi, R.; Lesbani, A. Effect of Ti^{4+}/clay ratio on the properties of titanium pillared bentonite and its application for Cr (VI) removal. *Rasayan J. Chem.* **2018**, *11*, 1244–1254. [CrossRef]
145. Belver, C.; Hinojosa, M.; Bedia, J.; Tobajas, M.; Alvarez, M.A.; Rodríguez-González, V.; Rodrigue, J.J. Ag-Coated Heterostructures of ZnO-TiO$_2$/DelaminatedMontmorillonite as Solar Photocatalysts. *Materials* **2017**, *10*, 960. [CrossRef]
146. Ökte, A.N.; Tuncel, D.; Pekcan, A.H.; Özden, T. Characteristics of iron-loaded TiO$_2$-supported montmorillonite catalysts: β-Naphthol degradation under UV-A irradiation. *J. Chem. Technol. Biotechnol.* **2014**, *89*, 1155–1167. [CrossRef]
147. Dali, A.; Rekkab-Hammoumraoui, I.; El Korso, S.; Boudjema, S.; Choukchou-Braham, A. Ruthenium-doped titania-pillared clay for the selective catalytic oxidation of cyclohexene: Influence of RU loading. *Bull. Chem. React. Eng. Catal.* **2019**, *14*, 614–624. [CrossRef]
148. Silva, A.S.; Kalmakhanova, M.S.; Massalimova, B.K.; de Tuesta, J.L.D.; Gomes, H.T. Wet peroxide oxidation of paracetamol using acid activated and Fe/Co-pillared clay catalysts prepared from natural clays. *Catalysts* **2019**, *9*, 705. [CrossRef]
149. Widjaya, R.R.; Saridewi, N.; Putri, A.A.; Rinaldi, N.; Dwiatmoko, A.A. Fe-Cr pillared clay as catalysts for the ethanol to gasoline conversion. In *IOP Conference Series: Materials Science and Engineering*; IOP Publishing: Bristol, UK, 2021; Volume 1011. [CrossRef]
150. Marković, M.; Marinović, S.; Mudrinić, T.; Ajduković, M.; Jović-Jovičić, N.; Mojović, Z.; Orlić, J.; Milutinović-Nikolić, A.; Banković, P. Co(II) impregnated Al(III)-pillared montmorillonite–Synthesis, characterization and catalytic properties in Oxone® activation for dye degradation. *Appl. Clay Sci.* **2019**, *182*, 105276. [CrossRef]
151. Chmielarz, L.; Gil, B.; Kuśtrowski, P.; Piwowarska, Z.; Dudek, B.; Michalik, M. Montmorillonite-based porous clay heterostructures (PCHs) intercalated with silica-titania pillars-synthesis and characterization. *J. Solid State Chem.* **2009**, *182*, 1094–1104. [CrossRef]
152. Rubiyanto, D.; Prakoso, N.I.; Sahroni, I.; Nurillahi, R. ZnO-Porous Clay Heterostructure from Saponite as Green Catalyst for Citronellal Cyclization. *Bull. Chem. React. Eng. Catal.* **2020**, *15*, 137–145. [CrossRef]
153. Belver, C.; Han, C.; Rodriguez, J.J.; Dionysiou, D.D. Innovative W-doped titanium dioxide anchored on clay for photocatalytic removal of atrazine. *Catal. Today* **2017**, *280*, 21–28. [CrossRef]
154. Jia, H.; Wang, C. Comparative studies on montmorillonite-supported zero-valent iron nanoparticles produced by different methods: Reactivity and stability. *Environ. Technol.* **2013**, *34*, 25–33. [CrossRef] [PubMed]
155. Mekewi, M.A.; Darwish, A.S.; Amin, M.S.; Eshaq, G.; Bourazan, H.A. Copper nanoparticles supported onto montmorillonite clays as efficient catalyst for methylene blue dye degradation. *Egypt. J. Pet.* **2016**, *25*, 269–279. [CrossRef]
156. Dhakshinamoorthy, A.; Pitchumani, K. Clay entrapped nickel nanoparticles as efficient and recyclable catalysts for hydrogenation of olefins. *Tetrahedron Lett.* **2008**, *49*, 1818–1823. [CrossRef]
157. Makwana, D.; Dakhara, B.; Bajaj, H.C.; Parmar, D.; Kumar, S.; Dhakhda, S.; Oza, M.D. Montmorillonite Clay Supported Palladium Nanoparticle for the Catalytic Hydrogenation of Furfural to Tetrahydrofurfuryl Alcohol. *Int. J. Eng. Res. Technol.* **2019**, *8*, 65–71.
158. Kahangi, F.G.; Mehrdad, M.; Heravi, M.M.; Sadjadi, S. Bio-assisted synthesized Ag(0) nanoparticles stabilized on hybrid of sepiolite and chitin: Efficient catalytic system for xanthene synthesis. *Sci. Rep.* **2020**, *10*, 15285. [CrossRef] [PubMed]

159. Bagchi, B.; Thakur, P.; Kool, A.; Das, S.; Nandy, P. In situ synthesis of environmentally benign montmorillonite supported composites of Au/Ag nanoparticles and their catalytic activity in the reduction of p-nitrophenol. *RSC Adv.* **2014**, *4*, 61114–61123. [CrossRef]

160. Wang, N.; Xiao, F.; Zhang, J.; Zhou, H.; Qin, Y.; Pan, D. Spherical montmorillonite-supported nano-silver as a self-sedimentary catalyst for methylene blue removal. *Appl. Clay Sci.* **2019**, *174*, 146–151. [CrossRef]

161. Zhao, X.F.; Liu, Z.L.; Li, X.D.; Li, S.P.; Song, F.G. The performance of attapulgite hybrids combined with MTX and Au nanoparticles. *J. Phys. Chem. Solids* **2019**, *124*, 73–80. [CrossRef]

162. Xiao, F.; Qin, Y.; Wang, N.; Pan, D. Towards mass production of Au nanoparticles supported on montmorillonite microspheres for catalytic reduction of 4-nitrophenol. *Appl. Clay Sci.* **2018**, *166*, 74–79. [CrossRef]

163. Belova, V.; Möhwald, H.; Shchukin, D.G. Sonochemical intercalation of preformed gold nanoparticles into multilayered clays. *Langmuir* **2008**, *24*, 9747–9753. [CrossRef] [PubMed]

164. Sohrabnezhad, S.; Rassa, M.; Seifi, A. Green synthesis of Ag nanoparticles in montmorillonite. *Mater. Lett.* **2016**, *168*, 28–30. [CrossRef]

165. Hariram, M.; Ganesan, V.; Muthuramkumar, S.; Vivekanandhan, S. Functionalization of kaolin clay with silver nanoparticles by Murraya koenigii fruit extract-mediated bioreduction process for antimicrobial applications. *J. Aust. Ceram. Soc.* **2021**, *57*, 505–513. [CrossRef]

166. Moradi, F.; Sedaghat, S.; Arab-Salmanabadi, S.; Moradi, O. Biosynthesis of silver-montmorillonite nanocomposites using Ocimum Basilicum and Teucrium Polium; A comparative study. *Mater. Res. Express* **2019**, *6*, 125008. [CrossRef]

167. Sheikh-Mohseni, M.H.; Sedaghat, S.; Derakhshi, P.; Safekordi, A. Green bio-synthesis of Ni/montmorillonite nanocomposite using extract of Allium jesdianum as the nano-catalyst for electrocatalytic oxidation of methanol. *Chin. J. Chem. Eng.* **2020**, *28*, 2555–2565. [CrossRef]

168. Das, T.K.; Ganguly, S.; Bhawal, P.; Remanan, S.; Mondal, S.; Das, N.C. Mussel inspired green synthesis of silver nanoparticles-decorated halloysite nanotube using dopamine: Characterization and evaluation of its catalytic activity. *Appl. Nanosci.* **2018**, *8*, 173–186. [CrossRef]

169. Wu, E.M.-Y.; Kuo, S.-L. Decolourization of Methylene Blue in Water Using Bentonite Impregnated with Ti and Ag as Photocatalyst. *Water Environ. Res.* **2015**, *87*, 727–734. [CrossRef]

170. Kaloidas, V.; Koufopanos, C.A.; Gangas, N.H.; Papayannakos, N.G. Scale-up studies for the preparation of pillared layered clays at 1 kg per batch level. *Microporous Mater.* **1995**, *5*, 97–106. [CrossRef]

171. Bertella, F.; Pergher, S.B.C. Scale up pillaring: A study of the parameters that influence the process. *Materials* **2017**, *10*, 712. [CrossRef] [PubMed]

172. Muñoz, H.J.; Vallejo, C.; Blanco, C.; Gil, A.; Vicente, M.Á.; Ramírez, J.H.; Galeano, L.A. 10 kg scaled-up preparation of Al/Fe-pillared clay CWPO catalysts from concentrated precursors. *Green Chem.* **2018**, *20*, 5196–5208. [CrossRef]

173. Li, Z.; Pan, Z.; Wang, Y. Mechanochemical preparation of ternary polyethyleneimine modified magnetic illite/smectite nanocomposite for removal of Cr(VI) in aqueous solution. *Appl. Clay Sci.* **2020**, *198*, 105832. [CrossRef]

174. Ravichandran, K.; Praseetha, P.K.; Arun, T.; Gobalakrishnan, S. *Synthesis of Nanocomposites*; Elsevier: Amsterdam, The Netherlands, 2018; ISBN 9780081019757.

175. Yang, R.; Cai, J.; Yang, H. Enhanced reactivity of zero-valent aluminum/O_2 by using Fe-bearing clays in 4-chlorophenol oxidation. *Sci. Total Environ.* **2021**, *773*, 145661. [CrossRef]

176. Foroughi, M.M.; Pardakhty, A.; Ranjbar, M. Simple Microwave Synthesis of CdO/Clay Nanocomposites and Investigation its Application for Degradation of MB. *J. Clust. Sci.* **2017**, *28*, 1685–1692. [CrossRef]

177. Sun, Y.; Zhang, P.; Hu, J.; Liu, B.; Yang, J.; Liang, S.; Xiao, K.; Hou, H. A review on microwave irradiation to the properties of geopolymers: Mechanisms and challenges. *Constr. Build. Mater.* **2021**, *294*, 123491. [CrossRef]

178. Barakan, S.; Aghazadeh, V. Synthesis and characterization of hierarchical porous clay heterostructure from Al, Fe-pillared nano-bentonite using microwave and ultrasonic techniques. *Microporous Mesoporous Mater.* **2019**, *278*, 138–148. [CrossRef]

179. Nain, S.; Singh, R.; Ravichandran, S. Importance of Microwave Heating In Organic Synthesis. *Adv. J. Chem. A* **2019**, *2*, 94–104. [CrossRef]

180. Hao, M.; Gao, P.; Liu, W.; Fang, B.; Liang, J.; Zhang, T.; Ding, Y.; Zhang, H.; Wang, F. Microwave hydrothermal-reduction synthesis of zanthoxylum trunk-like $Co/CoAl_2O_4$/sepiolite nanocomposite. *Ceram. Int.* **2021**, *47*, 4722–4728. [CrossRef]

181. Borah, B.; Dhar Dwivedi, K.; Kumar, B.; Raju Chowhan, L. Recent advances in the microwave- and ultrasound-assisted green synthesis of coumarin-heterocycles. *Arab. J. Chem.* **2021**, *15*, 103654. [CrossRef]

182. Olaya, A.; Blanco, G.; Bernal, S.; Moreno, S.; Molina, R. Synthesis of pillared clays with Al-Fe and Al-Fe-Ce starting from concentrated suspensions of clay using microwaves or ultrasound, and their catalytic activity in the phenol oxidation reaction. *Appl. Catal. B Environ.* **2009**, *93*, 56–65. [CrossRef]

183. Fuentes-García, J.A.; Santoyo-Salzar, J.; Rangel-Cortes, E.; Goya, G.F.; Cardozo-Mata, V.; Pescador-Rojas, J.A. Effect of ultrasonic irradiation power on sonochemical synthesis of gold nanoparticles. *Ultrason. Sonochem.* **2021**, *70*, 105274. [CrossRef] [PubMed]

184. Díez-García, M.I.; Manzi-Orezzoli, V.; Jankulovska, M.; Anandan, S.; Bonete, P.; Gómez, R.; Lana-Villarreal, T. Effects of Ultrasound Irradiation on the Synthesis of Metal Oxide Nanostructures. *Phys. Procedia* **2015**, *63*, 85–90. [CrossRef]

185. Pradisty, N.A.; Sihombing, R.; Howe, R.F.; Krisnandi, Y.K. Fe(III) Oxide-modified Indonesian Bentonite for Catalytic Photodegradation of Phenol in Water. *Makara J. Sci.* **2017**, *21*, 5. [CrossRef]

186. Sun, Z.; Feng, L.; Fang, G.; Chu, L.; Zhou, D.; Gao, J. Nano Fe_2O_3 embedded in montmorillonite with citric acid enhanced photocatalytic activity of nanoparticles towards diethyl phthalate. *J. Environ. Sci.* **2021**, *101*, 248–259. [CrossRef] [PubMed]

187. Nogueira, F.G.E.; Lopes, J.H.; Silva, A.C.; Lago, R.M.; Fabris, J.D.; Oliveira, L.C.A. Catalysts based on clay and iron oxide for oxidation of toluene. *Appl. Clay Sci.* **2011**, *51*, 385–389. [CrossRef]

188. Fang, L.; Hong, R.; Gao, J.; Gu, C. Degradation of bisphenol A by nano-sized manganese dioxide synthesized using montmorillonite as templates. *Appl. Clay Sci.* **2016**, *132–133*, 155–160. [CrossRef]

189. Kalidhasan, S.; Dror, I.; Berkowitz, B. Atrazine degradation through PEI-copper nanoparticles deposited onto montmorillonite and sand. *Sci. Rep.* **2017**, *7*, 1415. [CrossRef] [PubMed]

190. Tepmatee, P.; Siriphannon, P. Facile preparation of copper impregnated aluminum pillared montmorillonite: Nanoclays for wastewater treatment. *Bull. Pol. Acad. Sci. Tech. Sci.* **2016**, *64*, 553–560. [CrossRef]

191. John, M.; Jeffrey, B.; Thabang, N. Influence of operational parameters and kinetic modelling of catalytic wet air oxidation of phenol by al/zr pillared clay catalyst. *Iran. J. Chem. Chem. Eng.* **2019**, *38*, 189–203.

192. Kibanova, D.; Trejo, M.; Destaillats, H.; Cervini-Silva, J. Synthesis of hectorite–TiO_2 and kaolinite–TiO_2 nanocomposites with photocatalytic activity for the degradation of model air pollutants. *Appl. Clay Sci.* **2009**, *42*, 563–569. [CrossRef]

193. Li, X.; Peng, K.; Chen, H.; Wang, Z. TiO_2 nanoparticles assembled on kaolinites with different morphologies for efficient photocatalytic performance. *Sci. Rep.* **2018**, *8*, 11663. [CrossRef]

194. Djellabi, R.; Ghorab, M.F.; Cerrato, G.; Morandi, S.; Gatto, S.; Oldani, V.; Di Michele, A.; Bianchi, C.L. Photoactive TiO_2-montmorillonite composite for degradation of organic dyes in water. *J. Photochem. Photobiol. A Chem.* **2015**, *295*, 57–63. [CrossRef]

195. Wang, J.; Zhao, X.; Wu, F.; Tang, Z.; Zhao, T.; Niu, L.; Fang, M.; Wang, H.; Wang, F. Impact of montmorillonite clay on the homo- and heteroaggregation of titanium dioxide nanoparticles ($nTiO_2$) in synthetic and natural waters. *Sci. Total Environ.* **2021**, *784*, 147019. [CrossRef]

196. Fatimah, I.; Nurillahi, R.; Sahroni, I.; Muraza, O. TiO_2-pillared saponite and photosensitization using a ruthenium complex for photocatalytic enhancement of the photodegradation of bromophenol blue. *Appl. Clay Sci.* **2019**, *183*, 105302. [CrossRef]

197. Xiang, H.; Tuo, B.; Tian, J.; Hu, K.; Wang, J.; Cheng, J.; Tang, Y. Preparation and photocatalytic properties of Bi-doped TiO_2/montmorillonite composite. *Opt. Mater.* **2021**, *117*, 111137. [CrossRef]

198. Aritonang, A.B.; Pratiwi, E.; Warsidah, W.; Nurdiansyah, S.I.; Risko, R. Fe-doped TiO_2/Kaolinite as an antibacterial photocatalyst under visible light irradiation. *Bull. Chem. React. Eng. Catal.* **2021**, *16*, 293–301. [CrossRef]

199. Zhang, J.; Wang, S.; Xie, Y.; Gao, J. Characterization of N-doped TiO_2 pillared clay and its photocatalytic performance under visible light. *Chem. Eng. Trans.* **2018**, *71*, 217–222. [CrossRef]

200. Natsir, M.; Putri, Y.I.; Wibowo, D.; Maulidiyah, M.; Salim, L.O.A.; Azis, T.; Bijang, C.M.; Mustapa, F.; Irwan, I.; Arham, Z.; et al. Effects of Ni–TiO_2 Pillared Clay–Montmorillonite Composites for Photocatalytic Enhancement Against Reactive Orange Under Visible Light. *J. Inorg. Organomet. Polym. Mater.* **2021**, *31*, 3378–3388. [CrossRef]

201. Wang, W.K.; Chen, J.J.; Gao, M.; Huang, Y.X.; Zhang, X.; Yu, H.Q. Photocatalytic degradation of atrazine by boron-doped TiO_2 with a tunable rutile/anatase ratio. *Appl. Catal. B Environ.* **2016**, *195*, 69–76. [CrossRef]

202. Wang, J.; Liu, G.; Liu, Y.; Zhou, C.; Wu, Y. Photocatalytic Degradation of Methyl Orange by $Fe_2O_3-Fe_3O_4$ Nanoparticles and $Fe_2O_3-Fe_3O_4-$Montmorillonite Nanocomposites. *Clean* **2017**, *45*, 1600472. [CrossRef]

203. Ayodele, O.B.; Hameed, B.H. Synthesis of copper pillared bentonite ferrioxalate catalyst for degradation of 4-nitrophenol in visible light assisted Fenton process. *J. Ind. Eng. Chem.* **2013**, *19*, 966–974. [CrossRef]

204. Akkari, M.; Aranda, P.; Rhaiem, H.B.; Amara, A.B.H.; Ruiz-Hitzky, E. ZnO/clay nanoarchitectures: Synthesis, characterization and evaluation as photocatalysts. *Appl. Clay Sci.* **2016**, *131*, 131–139. [CrossRef]

205. Akkari, M.; Aranda, P.; Ben Haj Amara, A.; Ruiz-Hitzky, E. Organoclay hybrid materials as precursors of porous ZnO/silica-clay heterostructures for photocatalytic applications. *Beilstein J. Nanotechnol.* **2016**, *7*, 1971–1982. [CrossRef]

206. Fatimah, I.; Ardianti, S.; Sahroni, I.; Purwiandono, G.; Sagadevan, S.; Doong, R.A. Visible light sensitized porous clay heterostructure photocatalyst of zinc-silica modified montmorillonite by using tris(2,2′-bipyridyl) dichlororuthenium. *Appl. Clay Sci.* **2021**, *204*, 106023. [CrossRef]

207. Aguiar, J.E.; Cecilia, J.A.; Tavares, P.A.S.; Azevedo, D.C.S.; Castellón, E.R.; Lucena, S.M.P.; Silva, I.J. Adsorption study of reactive dyes onto porous clay heterostructures. *Appl. Clay Sci.* **2017**, *135*, 35–44. [CrossRef]

208. Junior, S.A.; de Sousa, J.F.; Benachour, M.; Rojas, L.O. Oxidacion Humeda de Fenoles con Catalizadores Fe-CeO_2, $KMnO_2$/CeO_2/Paligorsquita y Fe/Paligorsquita. *Inf. Technol.* **2011**, *22*, 55–68.

209. Gandía, L.M.; Vicente, M.A.; Gil, A. Complete oxidation of acetone over manganese oxide catalysts supported on alumina- and zirconia-pillared clays. *Appl. Catal. B Environ.* **2002**, *38*, 295–307. [CrossRef]

210. Kalmakhanova, M.S.; Diaz de Tuesta, J.L.; Kabykenovna, B.; Gomes, H.T. Pillared clays from natural resources as catalysts for catalytic wet peroxide oxidation: Characterization and kinetic insights. *Environ. Eng. Res.* **2020**, *25*, 186–196. [CrossRef]

211. Hadjltaief, H.B.; Zina, M.B.; Galvez, M.E.; Da Costa, P. Photo-Fenton oxidation of phenol over a Cu-doped Fe-pillared clay. *Comptes Rendus Chim.* **2015**, *18*, 1161–1169. [CrossRef]